Hindawi
Geofluids
Volume 2022, Article ID 8542453, 32 pages
https://doi.org/10.1155/2022/8542453

Research Article

Numerical Simulation on Hydrofracture Propagation in Fractured-Vuggy Unconventional Reservoirs

Tingxue Jiang[1,2], **Haitao Wang**[1,2], **Xiaobing Bian**[1,2], **Daobing Wang**[3], **Jun Zhou**[1,2] **and Bo Yu**[3]

[1]*State Key Laboratory of Shale Oil and Gas Enrichment Mechanisms and Effective Development, Beijing 102206, China*
[2]*SINOPEC Research Institute of Petroleum Engineering Co., Ltd., Beijing 102206, China*
[3]*School of Mechanical Engineering, Beijing Institute of Petrochemical Technology, Beijing 102617, China*

Correspondence should be addressed to Haitao Wang; wanght.sripe@sinopec.com and Daobing Wang; 0546wdb@163.com

Received 17 June 2022; Accepted 5 September 2022; Published 10 October 2022

Academic Editor: Dengke Liu

The unconventional reservoirs such as carbonate formation develops complex and diverse storage space structures, and it is composed of large-scale cavity, dissolved vug, and fractures. The carbonate reservoir is highly heterogeneous. Acid fracturing of carbonate reservoir is completed through the complex mechanical mechanism of interaction between vug and hydraulic fracture (HF). We use the equivalent method of reducing the rock strength by acid etching and serious fluid leakoff during interaction of HF and vug to establish a finite element (FE) model of HF propagation during acid fracturing in the fractured-vuggy carbonate reservoir. The model considers the effect of serious fluid leakoff during interaction between HF and vug, mechanism of interaction between HFs and the fracture-vug system, and change in acid etching intensity. Then, we carry out numerical simulation on impacts of injection rate, fluid viscosity, leakoff behavior in fractures and vugs, and natural fracture (NF) approaching angle on HF propagation in acid fracturing and compare the characteristics of injection pressure, fracture pressure, and HF size. It is suggested that the acid fracturing treatment should be operated by increasing the acid solution viscosity to reduce fluid leakoff, injecting fracturing fluid and acid fluid alternatively, increasing injection rate, and injecting fibers and ceramics when small pressure drop occurs during the HF interacts with the fracture-vug. When a large pressure drop occurs, it is suggested that the middle-low viscosity acid be injected at a low rate to etch the carbonate rock and enhance the fracture conductivity. HF propagates under higher pressure when the NF approaching angle is smaller.

1. Introduction

Abundant hydrocarbon is hosted in unconventional reservoirs such as the marine carbonate formation, and its exploration and development is a hot spot in the petroleum industry. Marine carbonate formations are widely developed in the platform in the Tarim Basin and cover about 30×10^4 km^2. Sinian-Ordovician carbonate rocks develop over 1,000 m longitudinally. Active tectonic movements and multistage of hydrocarbon charging provide favorable conditions for hydrocarbon accumulation. The paleo-uplift is favorable for hydrocarbon exploration and production [1]. The Ordovician carbonate formations in the basin are the karst fractured-vuggy type. After multistage tectonic movements, and weathering and denudation, and under effects of paleo-water systems, the complex and diverse reservoir spaces are developed, including large scale cavity, dissolved vugs, and fractures. The strong reservoir heterogeneity is formed [2]. Development of carbonate reservoirs faces problems such as low opening rate of producers, low cumulative production per well, and few high-production wells. Acid fracturing is a key technology to stimulate production in the fractured-vuggy carbonate reservoirs, and the study on HF propagation in these reservoirs is of great significance.

Experiments on HF propagation in the carbonate reservoirs have been reported a lot. HF propagation is affected by vugs, fracturing fluid type, in situ stress, and fracturing treatment parameters. Liu et al. [3] carried out experiments on HF propagation in the vuggy carbonate rock in a true

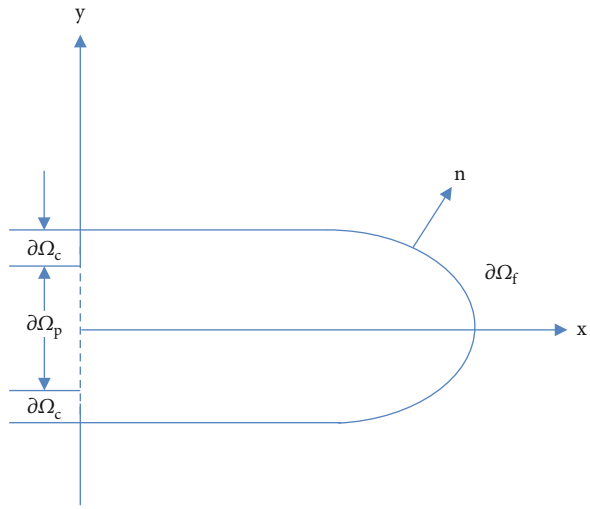

Figure 1: Fluid region boundary.

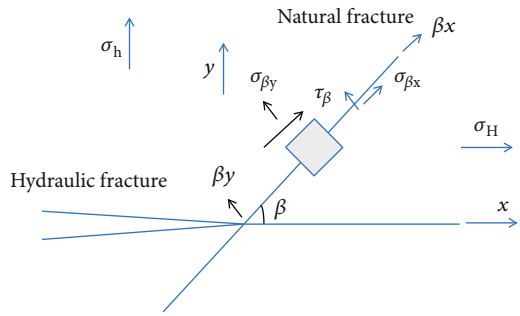

Figure 2: Interaction between HFs and NFs.

triaxial hydraulic fracturing system and acoustic emission monitoring of HF propagation. They suggested that vugs play a dominant role in HF propagation. The HF is interacted with vug through crossing small-scale vugs, arrest by large vugs, and bypassing vugs. The HF bypasses the vug under the condition of small horizontal stress difference. Interaction between HFs and vugs shows the obvious response in the fracturing curve. Guo et al. [4] carried out the true triaxial fracking test of carbonate samples with water, supercritical CO_2 and liquid CO_2, and CT scanning of HF morphology. The supercritical CO_2 increases the pore pressure in the carbonate rocks and reduces the fracture pressure due to its low viscosity, strong diffusivity and leak-off. Supercritical CO_2 fracturing of the carbonate rock needs more liquid injected compared with water fracturing. Tensile failure occurs in water and liquid CO_2 fracturing of carbonate rocks, and HF extends along the orientation of the maximum horizontal stress. Shear failure occurs in supercritical CO_2 fracturing, and HF propagation is less controlled by the stress anisotropy. Guo et al. [5] studied HF propagation in the carbonate rocks under fracturing fluid of various viscosity. The fluid viscosity has a great impact on the fracture pressure. The low-viscosity fluids activate and open more natural fractures (NFs), and the breakdown pressure is lowest. Gelled acid enhances the fracture width and improves the fracture conductivity.

Luo et al. [6] carried out experiments on HF propagation in carbonate rock samples with the preset NFs at the dip angle of 15°-90°, and HF initiation, NF propagation, multiple fracture connection, and NF closure were observed. Liu et al. [7] carried out experiments on the impacts of NF size and bulk density, and horizontal stress anisotropy on HF propagation in the carbonate rock samples. The results show that volumetric fractures are formed in the samples with developed NFs.

Gou et al. [8] performed physical simulation on HF propagation in true triaxial acid fracturing of 200 mm × 200 mm × 200 mm carbonate rock samples and compared the effects of nonreactive fluids such as water, guar gum, and acid fluid such as self-generating acid, gelled acid, and viscoelastic surfactant (VES) acid on HF propagation. CT scanning and 3D reconstruction of fracture morphology show that the acid promotes connection with NFs, and the HF formed by acid fracturing propagates along with the NFs and is not controlled by the maximum horizontal principal stress. Zhang et al. [9] carried out 3D scanning of HFs in the carbonate rocks after acid fracturing with VES acid

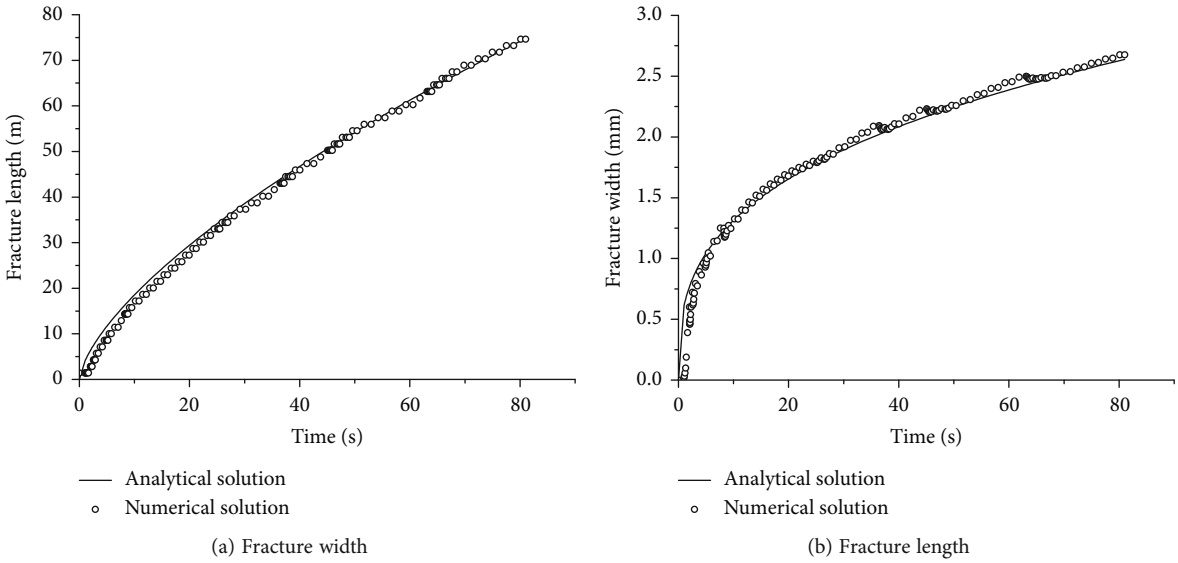

(a) Fracture width (b) Fracture length

Figure 3: FE and analytical solutions of the fracking model.

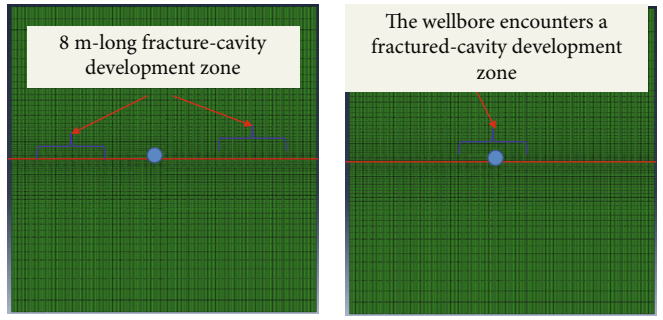

(a) Case 1 (b) Case 2

Figure 4: Physical model of fracture and vugs.

and gelled acid and found that the gelled acid reduces the rock compressive strength and Poisson's ratio, and the VES acid reduces the rock tensile strength and Young's modulus. The VES acid creates a rough fracture, and the gelled acid creates a groove-like fracture.

Hou et al. [10] carried out experiments on HF propagation in the compacted limestone by considering horizontal stress anisotropy, fluid viscosity, injection rate, and completion methods and observed transverse fractures, axial fractures, and complex fractures. Liu et al. [11] found in experiments that the lower horizontal principal stress difference $\Delta\sigma$ and the angle $\Delta\theta$ between the maximum horizontal principal stress and the NF are the main factors controlling HF initiation and propagation. When $\Delta\theta = 90^\circ$ and $\Delta\sigma \geq 2$ MPa or $\Delta\theta = 60^\circ$ and $\Delta\sigma \geq 4$ MPa, HF initiation and propagation direction is normal to the NFs. Dai et al. [12] studied HF propagation during acid fracturing in a true triaxial acid fracturing device. The results show that low-viscosity diverting acid promotes formation of the fracture network, and the fracture complexity is affected by NFs and pre-pad viscosity.

In numerical simulation, study on HF propagation during acid fracturing of the carbonate rock has been carried out by analytical solution, finite element method (FEM), extended finite element (XFEM) method, phase field, and proper generalized decomposition method. Qiao et al. [13] used TOUGH-AiFrac simulator to analyze the effects of NF strike, confining pressure, fluid pressure in vugs, and injection pressure on HF propagation in carbonate rocks. They found that NF and confining pressure have the greatest effect on HF propagation, and the vugs attract HF propagation. Chen et al. [14] built up a three-dimensional unified pipe network model for matrix acidizing process of naturally fractured carbonate formations, where the fractures and porous media are equivalently characterized by interconnected matrix pipes and fracture pipes, and they simulated the process of wormhole propagation during the acidizing process by integrating a dual-scale continuum model. Shovkun and Espinoza [15] studied the effect of mineral dissolution on 3D pore structure and HF propagation in the semicircular bending experiment on limestone in the acidizing process and performed simulation on tensile HF propagation

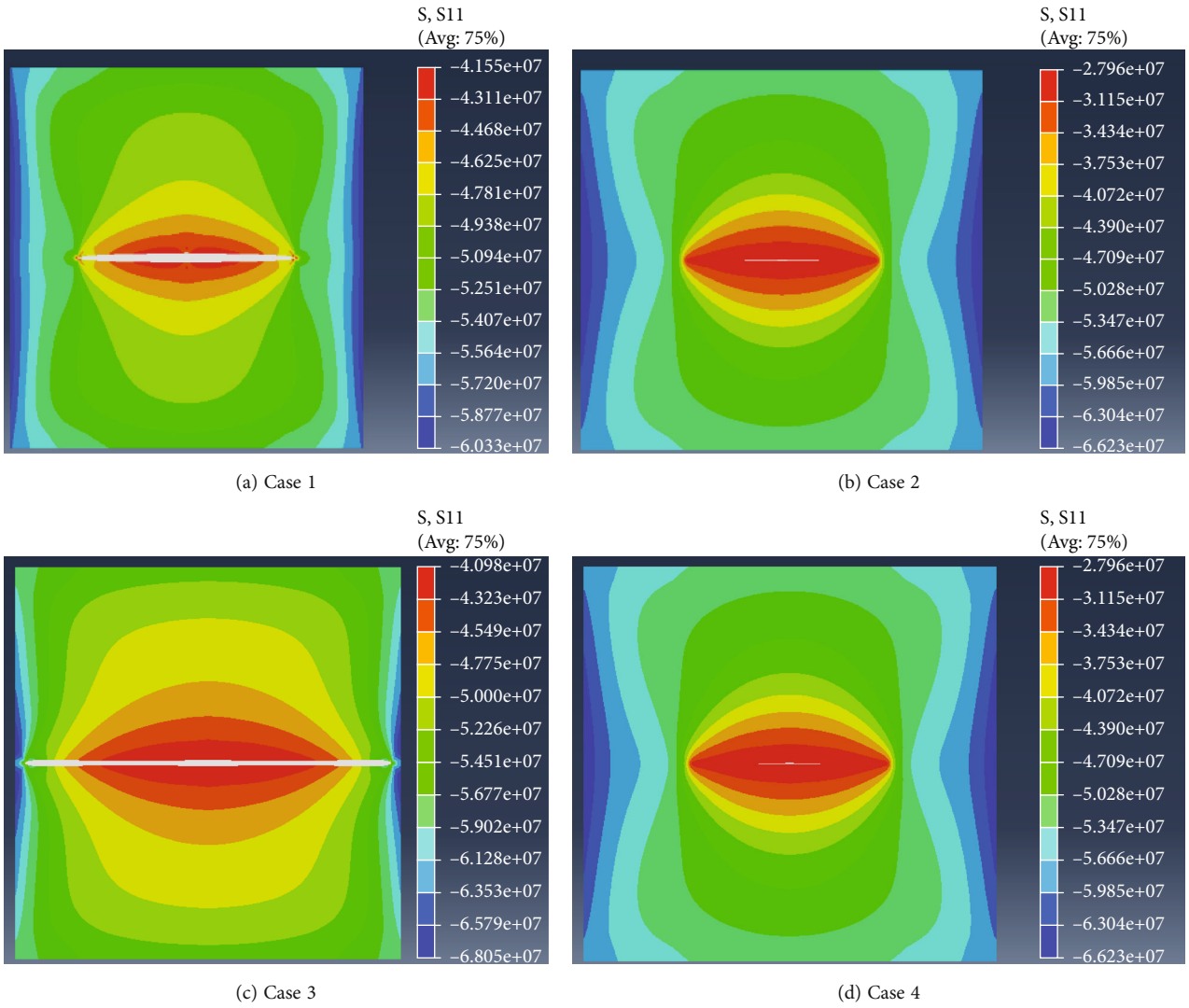

(a) Case 1 (b) Case 2

(c) Case 3 (d) Case 4

Figure 5: Contour map of stress S_{11} in Cases 1, 2, 3, and 4.

with the FEM based on the phase field model. Nonplanar fractures are formed in the high-porosity and large-channel regions. Shovkun and Espinoza [16] studied the effect of the reactive fluids on the weakening strength at the HF tip in the carbonate rock and analyzed the HF propagation characteristics where the fracture toughness dominates the mechanism and carried out numerical simulation based on phase field by considering fluid flow, poroelasticity, linear elastic fracture mechanics, and chemical reaction transport.

Ma et al. [17] established a thermal-mechanical-chemical coupling 3D unified pipe network model to simulate the matrix acidizing process in the fractured carbonate formations by extending the traditional dual-scale continuum model, considering thermal effects and multiple field-coupling governing equation, and discretizing the fracture network system with an equivalent compatible grid method. Subsequently, Ma et al. [18] applied the unified pipe network to establish a 3D dual-phase acidizing model for simulation of propagation of acidizing wormholes in the fractured carbonate formation, and obtained the solution by sequential implicit time and adaptive time step methods. Li et al. [19] studied fracture deformation and pressure distribution within a fracture in ANSYS software, and found that the NF intersected with the wellbore are very sensitive to pressure fluctuation within the wellbore and cause fluid leakoff in completion operation. Luo et al. [20] established an XFEM model by considering the effects of mechanical deformation, fluid flow, acid-rock reaction, vugs, NFs, and acid on HF propagation and performed a simulation of propagation of acid-etched fractures in fractured-vuggy carbonate rock. The numerical result has a good agreement with the solution from the typical Kristianovich-Geertsma-de Klerk (KGD) model. Based on the tensile failure criterion, Wang et al. [21] established a 2D analytical model of HF propagation during temporary plugging and diverting acid fracturing in carbonate rocks by considering the effect of rock permeability and injection pressure on the diversion radius. Subsequently, Wang et al. [22] applied the method of reduced spatial-temporal dimensions to establish a proper generalized

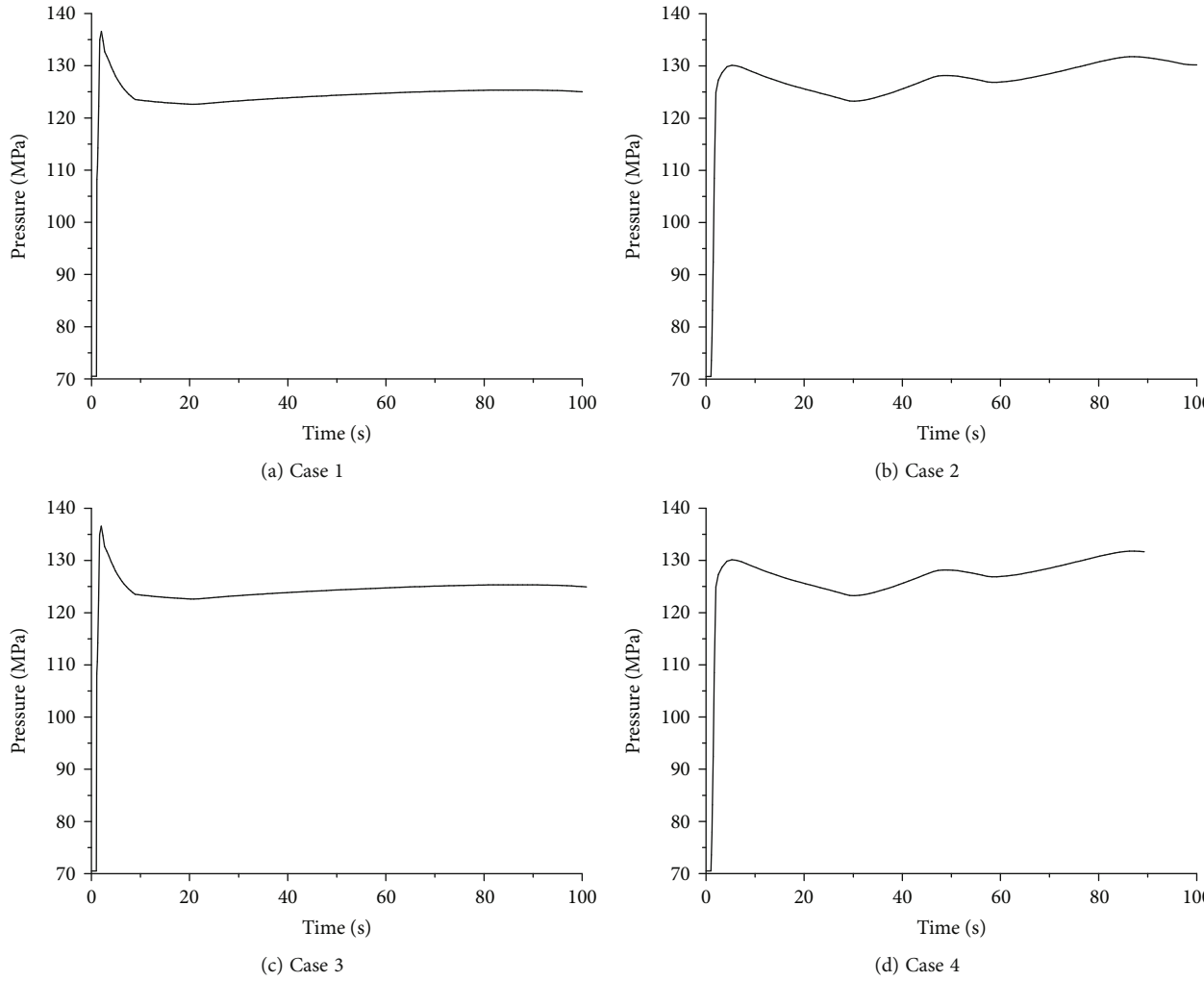

Figure 6: Injection pressure within the fracture in Cases 1, 2, 3, and 4.

decomposition algorithm for hydraulic fracturing, which decomposes the fluid-solid coupling problem into the differential equations as a function of temporal and spatial variables, and they solved the equations by alternative iteration algorithmn. Computation efficiency is over 10 times faster than that of the conventional FEM, and its solution has a good agreement with the FEM solution. Wang et al. [23] developed a constitutive model for temporary plugging based on spring elements by coupling rock failure and seepage flow in the rock mass. The HF network structure is established adaptively. The increase of the net pressure within the hydro-fracture during temporary plugging operation is simulated by activating the element when the diverter is added and deactivating the element when injection of the diverter is stopped. Recently, a damage mechanics-based FE model is established to simulate fracture propagation process in fracking of heterogenous reservoirs [24]. The Weibull random function is used to represent the degree of heterogeneity of mechanical properties. In addition, the embedded discrete fracture model is incorporated into the hydraulic fracturing simulator to calculate the acid fracturing process in carbonate reservoirs. This model realizes the coupling solution between fracture flow and seepage fluid in rock matrix and thus improves the computation efficiency with respect to the conventional fracking algorithm [25].

The cohesive zond based FEM simulation on HF propagation overcomes the defects in mesh refinement at the fracture tip in the conventional FEM. Nevertheless, the impact of acid etching on the mechanical strength and fluid leakoff is not considered. We use the equivalent method of reducing rock strength by acid etching and serious fluid leakoff during acid fluid communicating with vugs to establish the acid fracturing model by considering the permeability and porosity with the change of the confining pressure and dividing the carbonate rock into the acid-etched area and non-acid-etched area. Finally, we simulate the effects of fluid leakoff, interaction between vugs and HFs, and the approaching angle on HF propagation during acid fracturing in fractured-vuggy carbonate rock.

The structure of this paper is organized as follows. First, it gives the equations of fluid flow in HFs and fracture width, the equivalent acid fracturing model, and mechanical criteria of the interaction between the HF and NFs. Secondly, it carries out numerical simulation on HFs in the carbonate

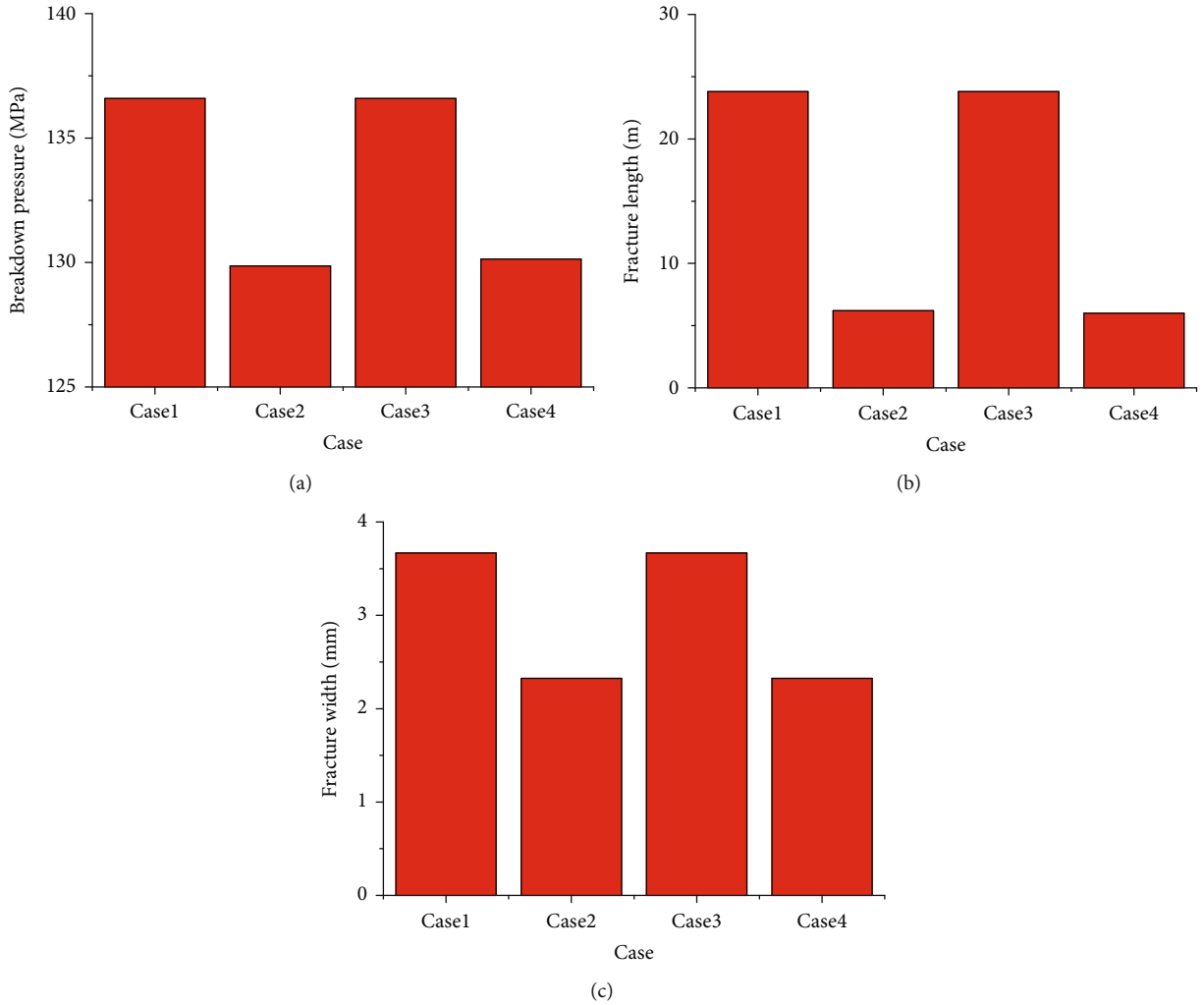

Figure 7: Breakdown pressure (a), fracture length (b), and fracture opening (c) in Cases 1, 2, 3, and 4.

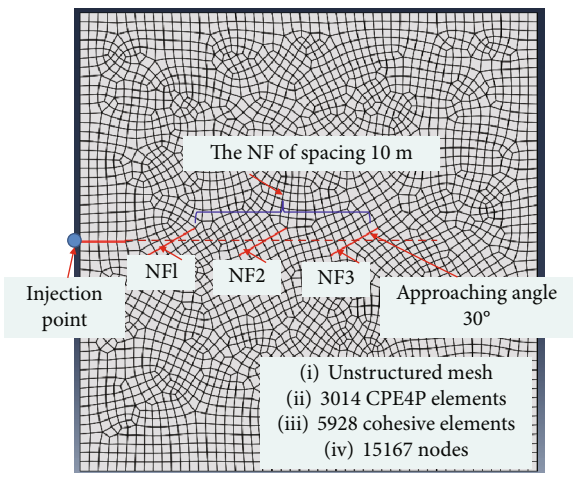

Figure 8: Physical model of three NFs intersected with one HF, where CPE4P elements represent a quadrilateral element with pore pressure.

Table 1: Input parameters of FE model.

Parameters	Value
Rock tensile strength	6 MPa
NF tensile strength	2 MPa
Equivalent elastic modulus	30 GPa
Equivalent Poisson ratio	0.25
Permeability	0.4 md
Porosity	1.0%
Horizontal principal stress anisotropy coefficient	0.1/0.2/0.3
Approaching angle	90°/60°/45°/30°
Liquid viscosity	10/30/50/100/200 mPa·s
Injection rate	1/2/4/6/8 m^3/min
Pore pressure	70.5 MPa
Reservoir thickness	50 m

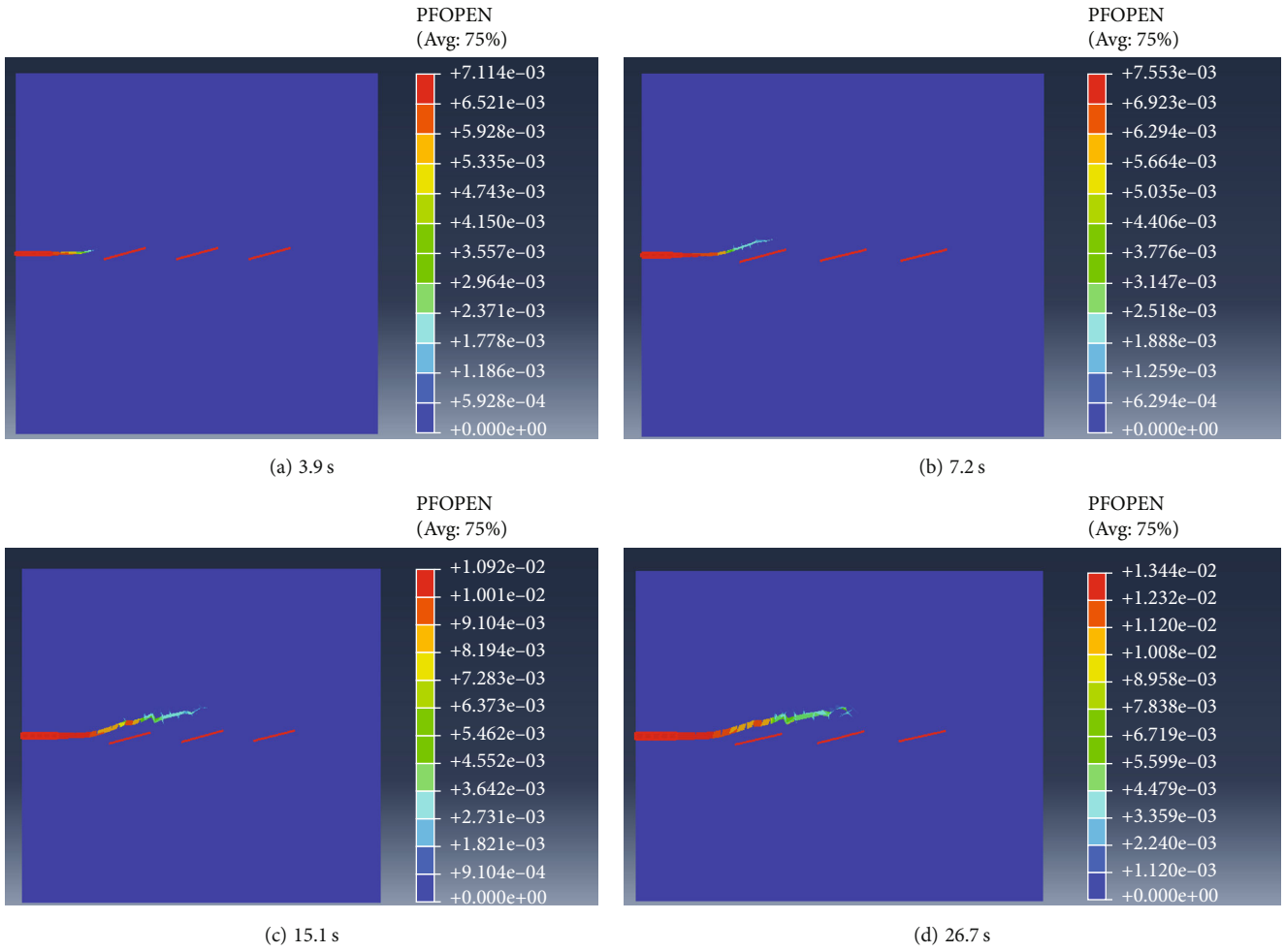

Figure 9: HF propagation at the NF approaching angle of 30° and stress anisotropy coefficient of 0.3, where PFOPEN in the legend represents fracture opening.

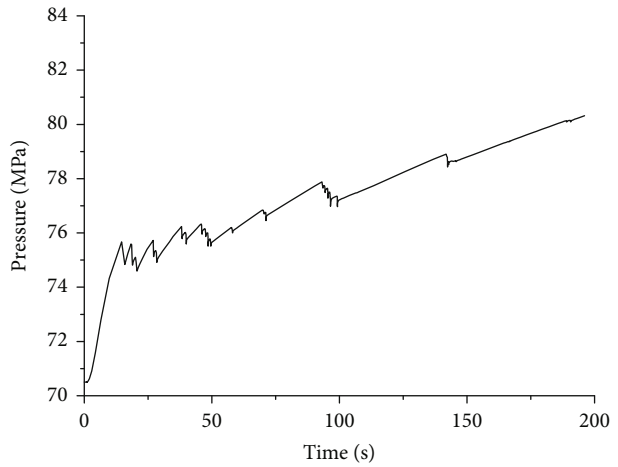

Figure 10: Pressure curve at the NF approaching angle of 30° and the stress anisotropy coefficient of 0.3.

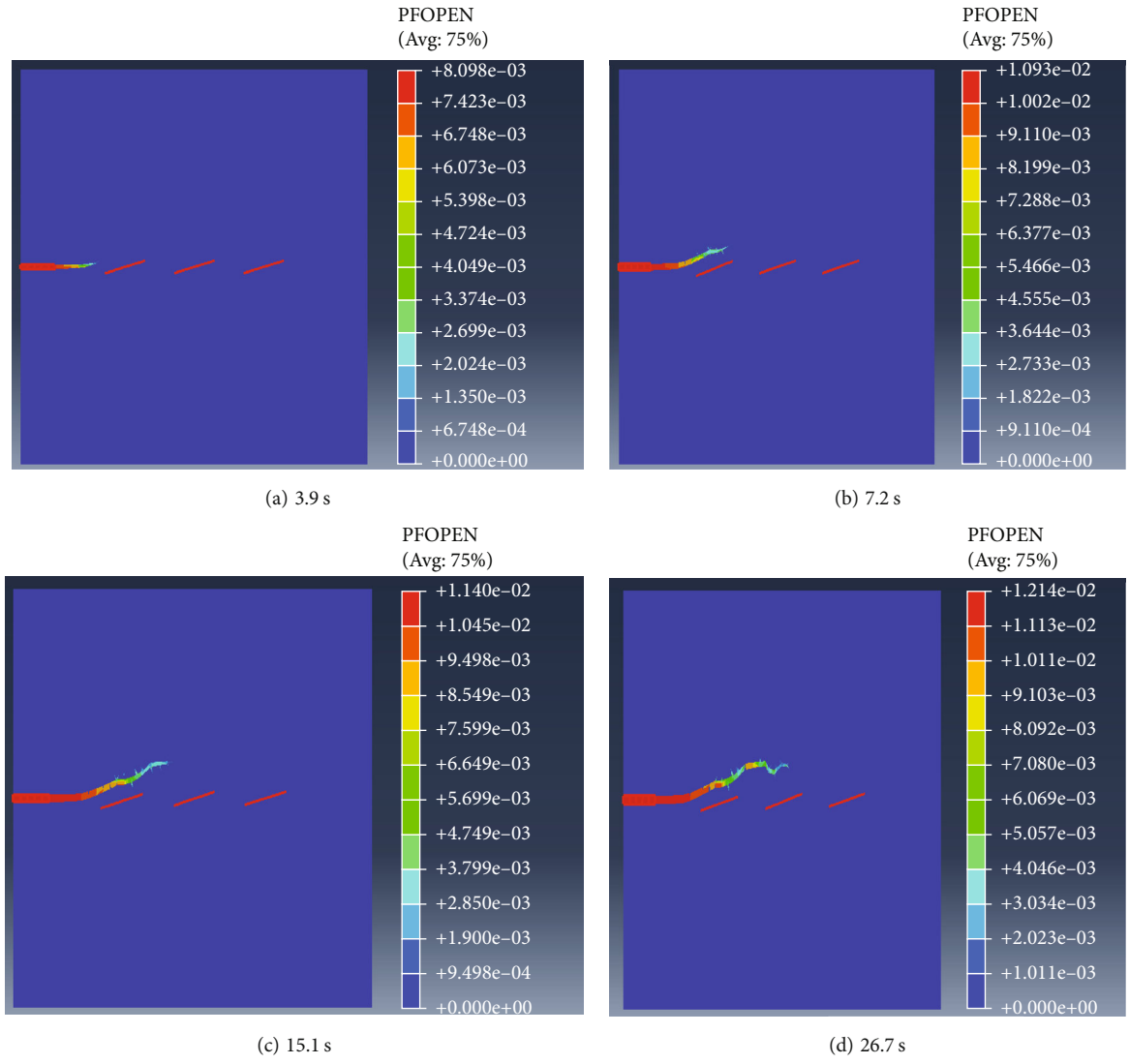

Figure 11: HF propagation at the NF approaching angle of 30° and stress anisotropy coefficient of 0.2.

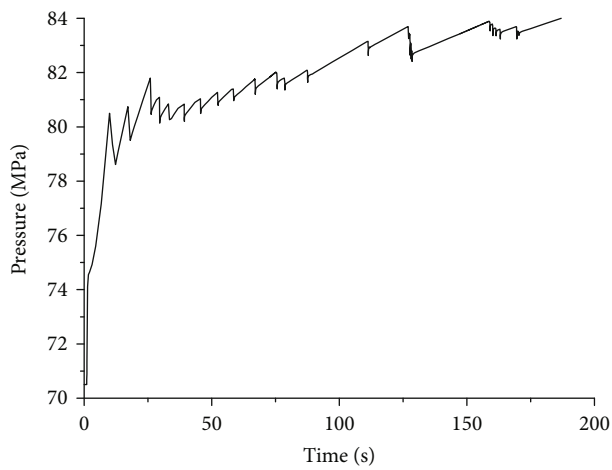

Figure 12: Pressure curve at the NF approaching angle of 30° and stress anisotropy coefficient of 0.2.

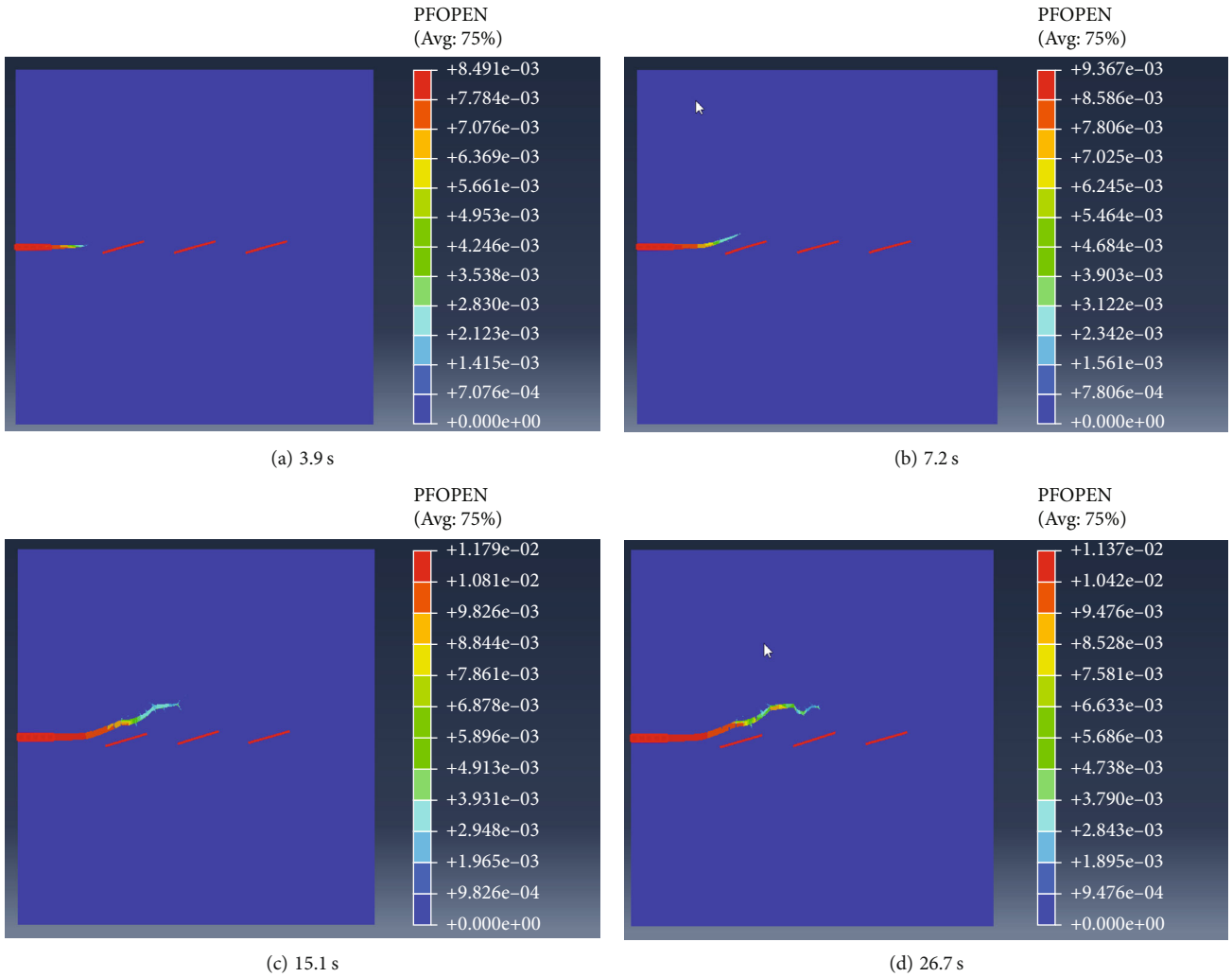

Figure 13: HF propagation at the NF approaching angle of 30° and stress anisotropy coefficient of 0.1.

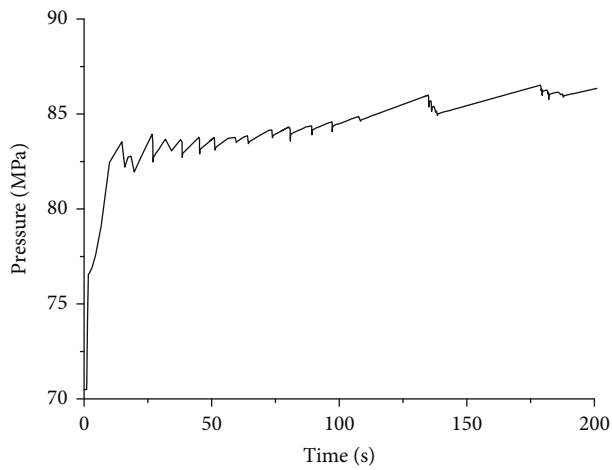

Figure 14: Pressure curve at the NF approaching angle of 30° and stress anisotropy coefficient of 0.1.

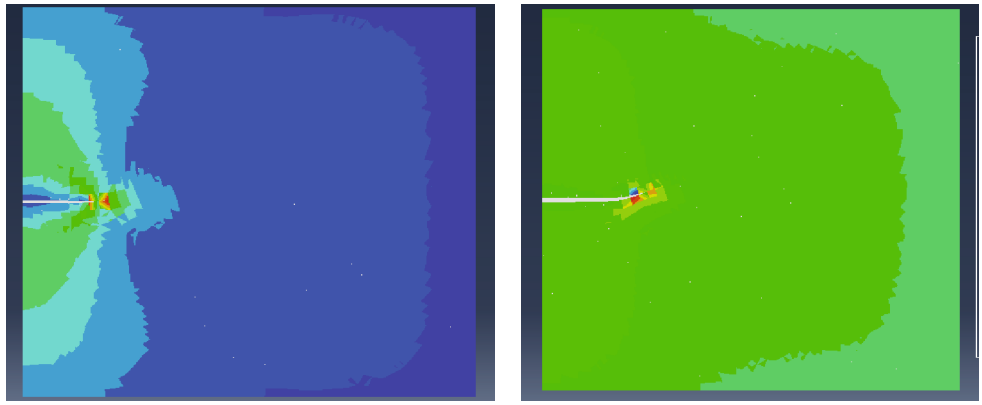

(a) 1 m^3/min (b) 2 m^3/min

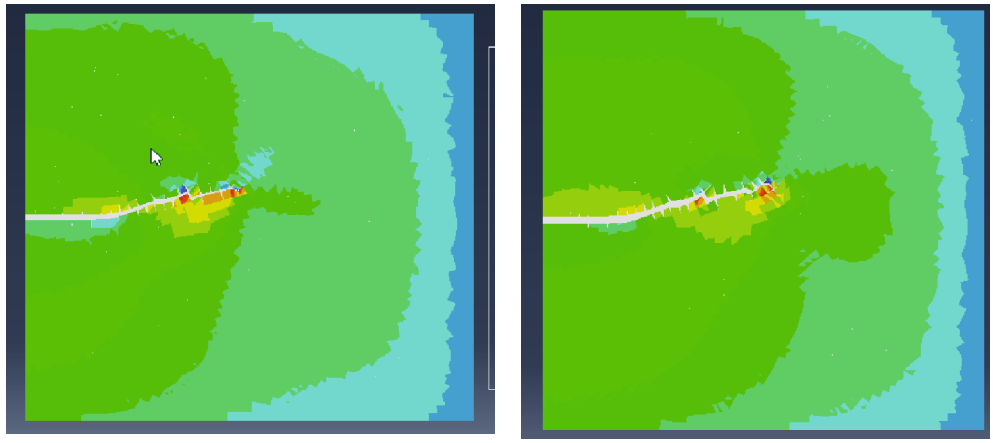

(c) 4 m^3/min (d) 6 m^3/min

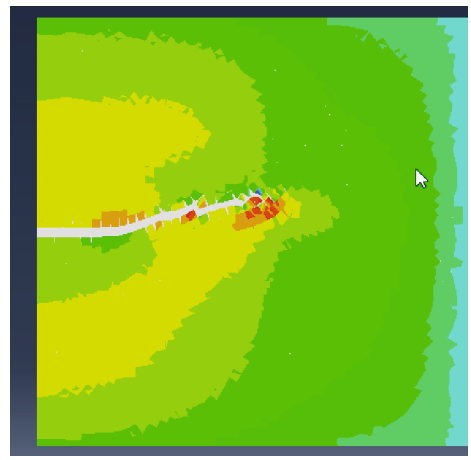

(e) 8 m^3/min

FIGURE 15: Contour map of stress component S_{11} at the NF approaching angle of 30° and at the rate of 1 m^3/min, 2 m^3/min, 4 m^3/min, 6 m^3/min, and 8 m^3/min.

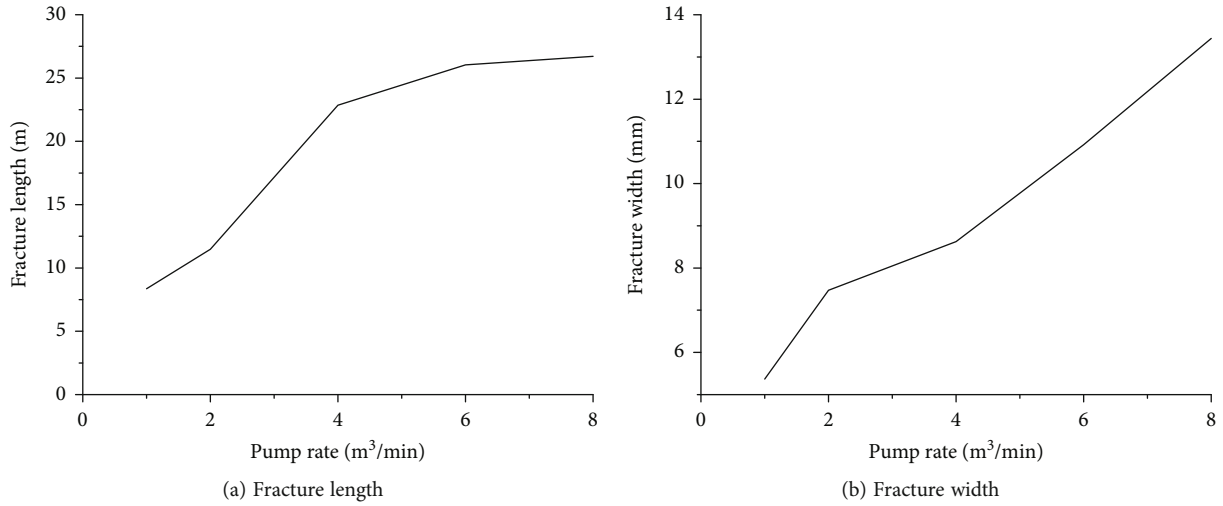

(a) Fracture length (b) Fracture width

Figure 16: Fracture length and width at the NF approaching angle of 30° and at injection rates from 1-8 m³/min.

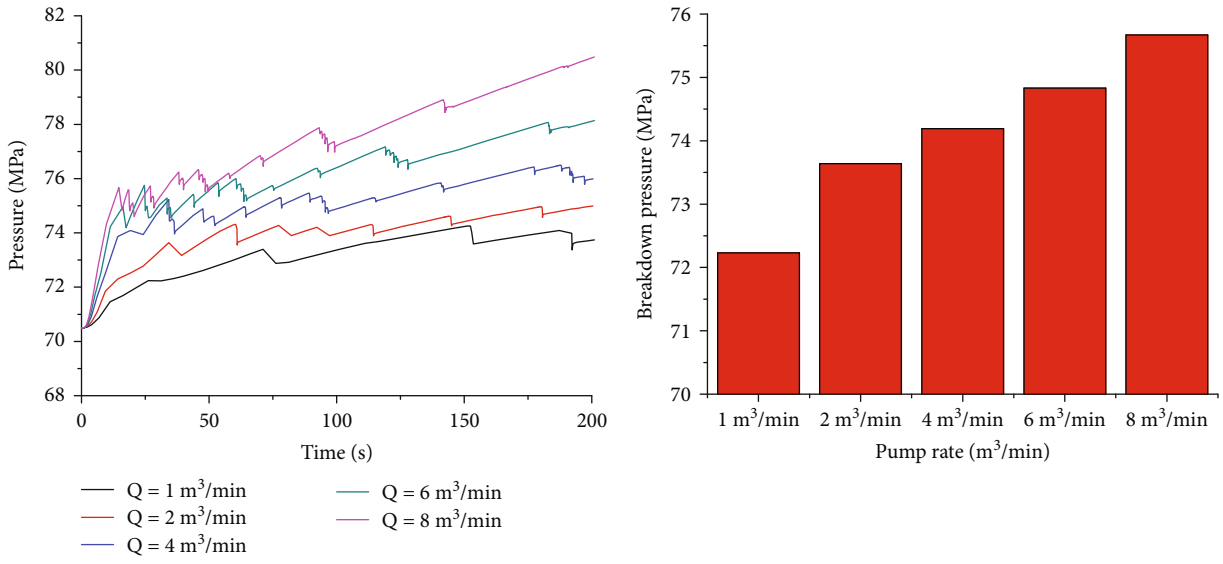

(a) Pressure within the fracture (b) Fracture pressure

Figure 17: Pressure within the fracture and fracture pressure at the NF approaching angle of 30° and at injection rates from 1-8 m³/min.

reservoir, analyzes fluid leakoff in the fracture-vug and the interaction between HFs and NFs, and gives comparison of breakdown pressure, injection pressure, fracture length, and fracture width. Finally, it describes the conclusions.

2. Theory and Method

2.1. Equation of Fluid Flow within the HF. We assume that the seepage flow within the hydrofracture is incompressible, a part of the injected liquid is used to create fractures, and the other part is leaked off into the rock matrix. According to the fluid mechanics, seepage flow in the hydro-fracture is expressed with the partial differential equation as follows [26]:

$$\frac{\partial}{\partial x}\left(\frac{w^3}{12\mu}\frac{\partial p}{\partial x}\right)+\frac{\partial}{\partial x}\left(\frac{w^3}{12\mu}\frac{\partial p}{\partial x}\right)=\frac{\partial w}{\partial t}+q_l,$$
$$q_l=\frac{2c_l}{\sqrt{t-\tau(x,y)}}. \tag{1}$$

Fluid flow at the entry of HF $\partial\Omega_p$ (Figure 1) is expressed as follows [24]:

$$-\frac{w^3}{12\mu}\frac{\partial p}{\partial n}=Q. \tag{2a}$$

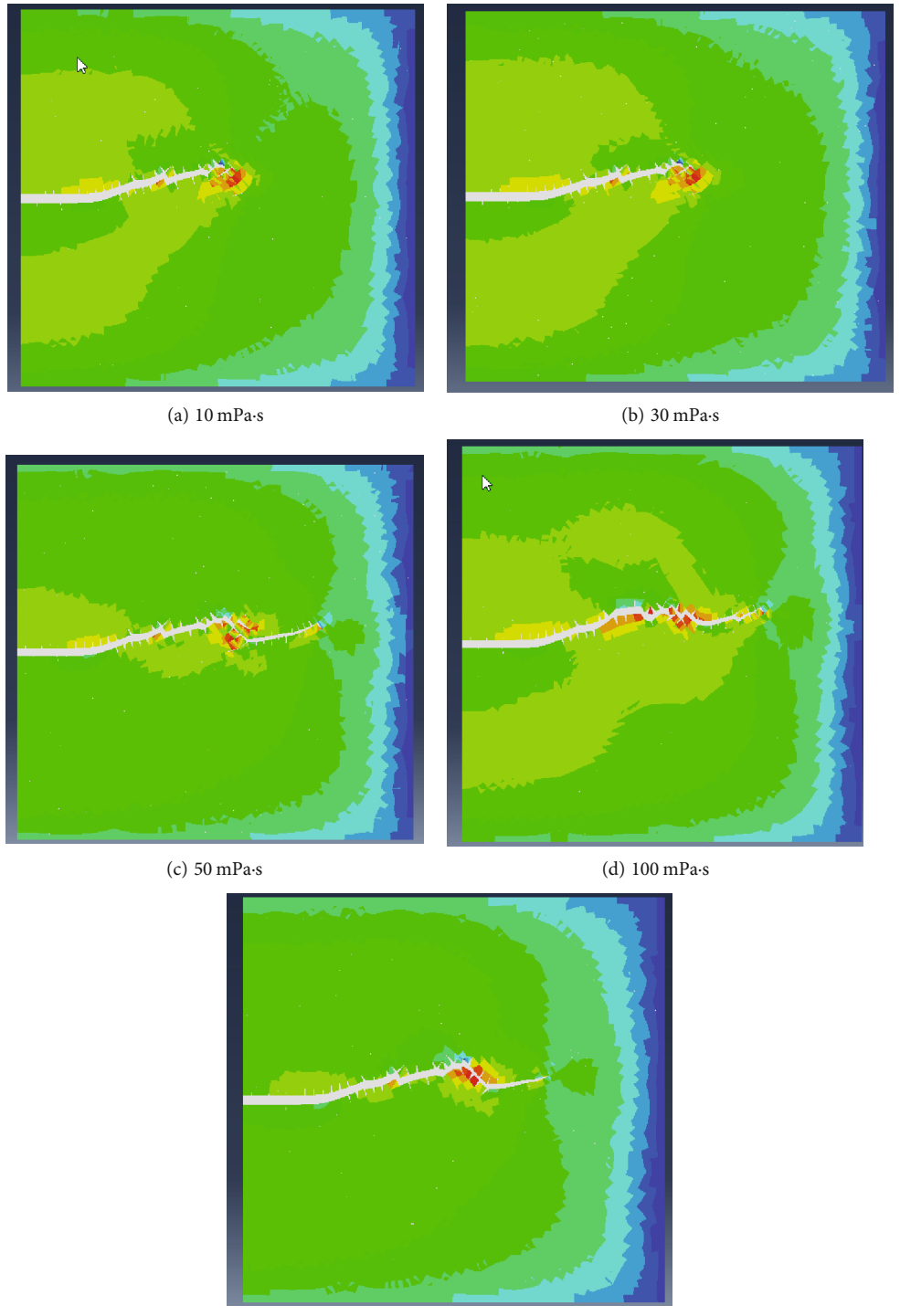

(a) 10 mPa·s (b) 30 mPa·s

(c) 50 mPa·s (d) 100 mPa·s

(e) 200 mPa·s

Figure 18: Stress contour map at the NF approaching angle of 30° and fluid viscosity of 10-200 mPa·s.

Fluid flow at the symmetrical sections $\partial\Omega_c$ is expressed as follows:

$$-\frac{w^3}{12\mu}\frac{\partial p}{\partial n}=0. \tag{2b}$$

Fluid flow at the fracture front $\partial\Omega_f$ is expressed as follows:

$$-\frac{w^3}{12\mu}\frac{\partial p}{\partial n}=0. \tag{2c}$$

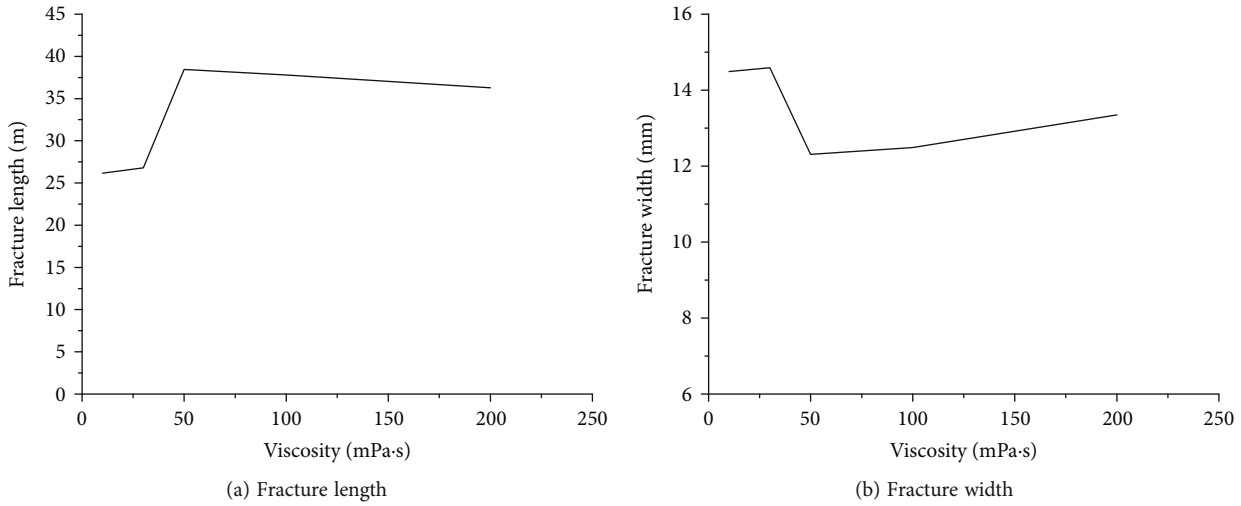

(a) Fracture length (b) Fracture width

Figure 19: Fracture length and width at the NF approaching angle of 30° and fluid viscosity of 10-200 mPa·s.

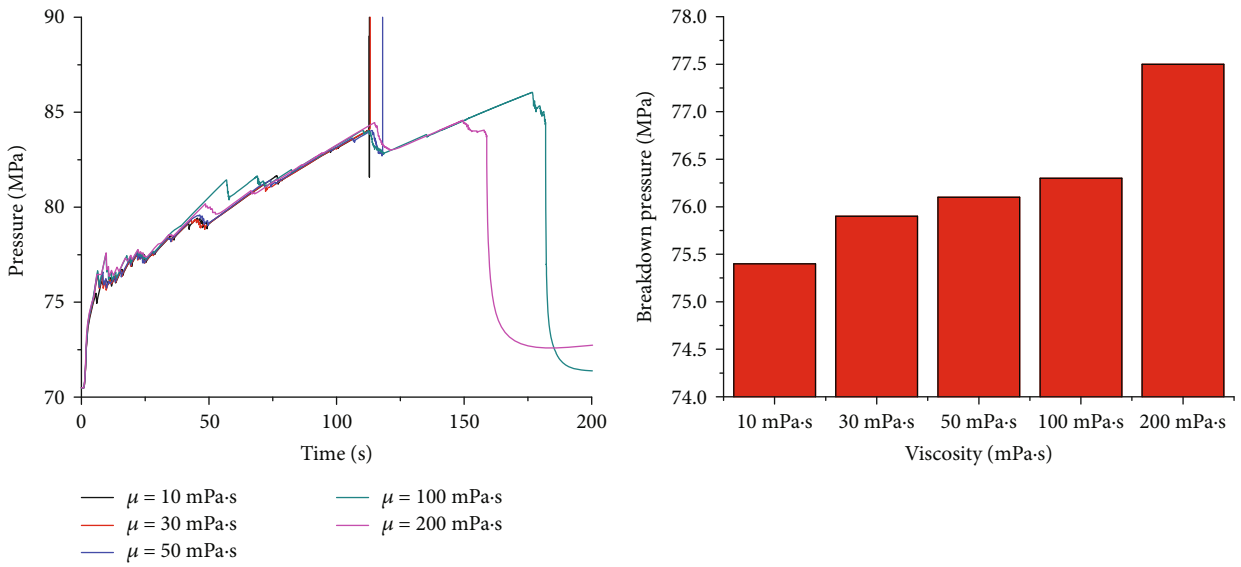

(a) Injection pressure (b) Fracture pressure

Figure 20: Injection pressure and fracture pressure at the NF approaching angle of 30° and fluid viscosity of 10-200 mPa·s.

2.2. Equation of Fracture Width. According to the elasticity theory, the fracture width is expressed as follows [26]:

$$T(x,y) = \frac{G}{4\pi(1-\nu)}\int_{\Omega}\left[\frac{\partial}{\partial x}\left(\frac{1}{r}\right)\frac{\partial w}{\partial x'} + \frac{\partial}{\partial y}\left(\frac{1}{r}\right)\frac{\partial w}{\partial y'}\right]dx'dy', \tag{3}$$

$$r = \left[\left(x-x'\right)^2 + \left(y-y'\right)^2\right]^{1/2}, \tag{4}$$

$$T(x,y) = -[p(x,y) - \sigma_{\min}(x,y)], \tag{5}$$

We assume that $v(x,y)$ is a test function, which satisfies the zero displacements at the fracture front. We multiply by $v(x,y)$ and integrate on both sides of Equation (3). Then, we have the following [26]:

$$\int_{\Omega} T(x,y)v(x,y)dxdy = \frac{G}{4\pi(1-\nu)}\int_{\Omega}\int_{\Omega}\frac{1}{r}\left(\frac{\partial v}{\partial x}\frac{\partial w}{\partial x'} + \frac{\partial v}{\partial y}\frac{\partial w}{\partial y'}\right)dxdydx'dy'. \tag{6}$$

2.3. Equivalent Acid Fracturing Model. During acid fracturing, the carbonate rock is divided into acid-etched areas and non-acid-etched areas. The governing equations of HF propagation during acid fracturing of carbonate rocks integrate stress equilibrium, pressure in pores and flow pressure in fractures.

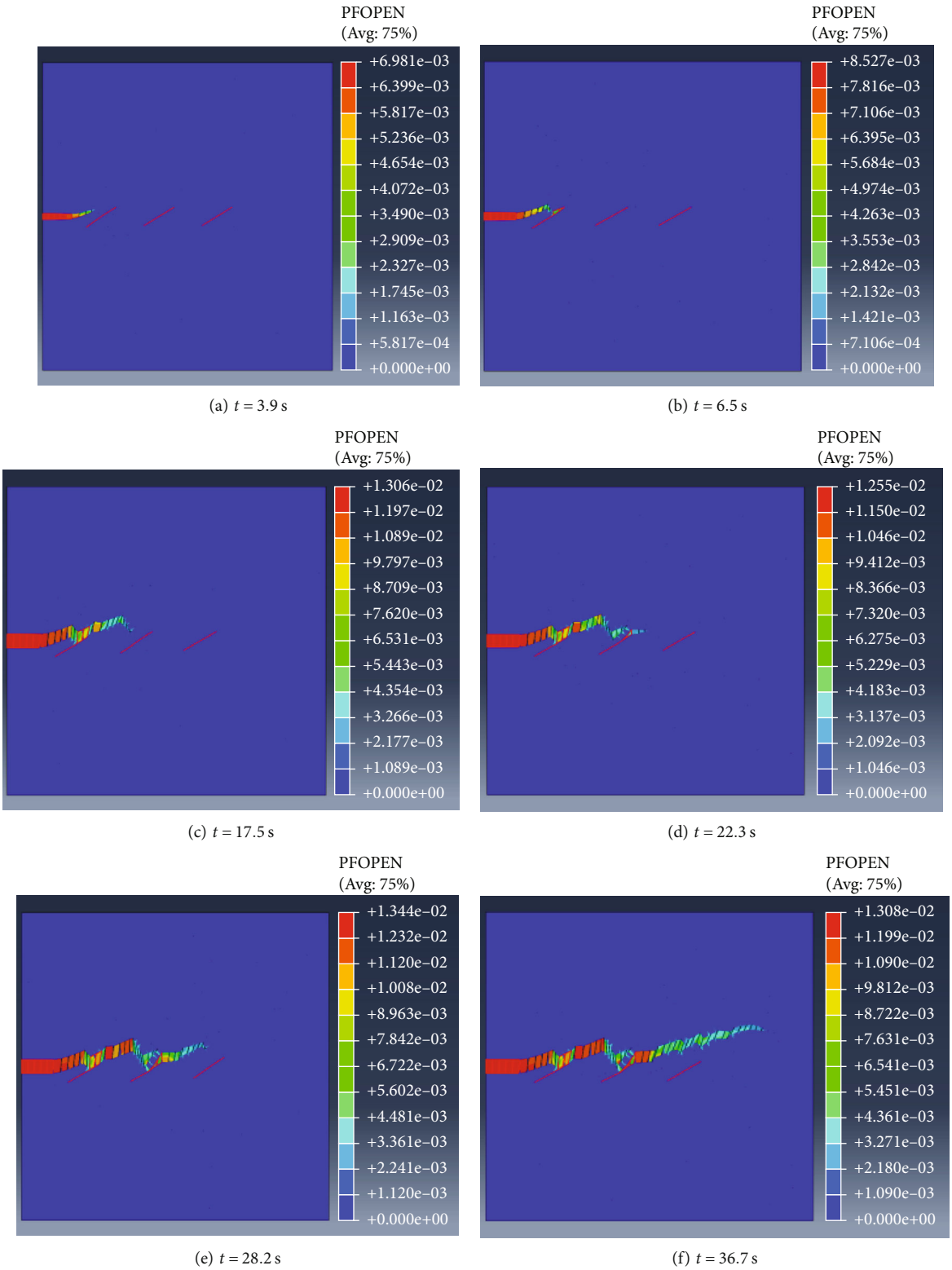

(a) $t = 3.9$ s (b) $t = 6.5$ s

(c) $t = 17.5$ s (d) $t = 22.3$ s

(e) $t = 28.2$ s (f) $t = 36.7$ s

Figure 21: HF propagation at the NF approaching angle of 45° and stress anisotropy coefficient of 0.3.

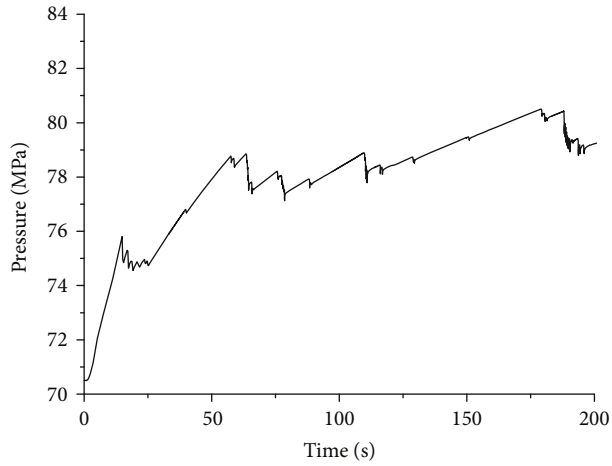

Figure 22: Pressure curve at the NF approaching angle of 45° and stress anisotropy coefficient of 0.3.

Different from the conventional hydraulic fracturing model, the acid fracturing model considers the fracture conductivity, rock porosity, and permeability under the confining pressure. The equations of fracture conductivity, rock porosity, and permeability with the change of closure pressure after acid etching are added to the equation system. The equations and boundary conditions are expressed as follows.

According to the theory of elasticity, the stress equilibrium in the rock matrix is written as follows:

$$\frac{\partial \sigma_{ij}}{\partial x_j} - \alpha \frac{\partial p}{\partial x_j} + f_i = 0. \tag{7}$$

The boundary condition is written as follows:

$$\begin{aligned} \sigma_{ij} n_j - t_i &= 0, \\ u_i &= \bar{u}_i. \end{aligned} \tag{8}$$

The pressure distribution in the rock matrix in the acid etching area is written as follows [27]:

$$-\nabla\left(\frac{k(\sigma_e)}{\mu}\nabla p\right) = C\varphi(\sigma_e)\frac{\partial p}{\partial t}. \tag{9}$$

The permeability and porosity are a function of the effective stress and changes with rock types and acid properties, etc. Then, the permeability is expressed as follows [25]:

$$k = k_0\left[1 - \left(\frac{\sigma}{\sigma_0}\right)^m\right]^3, \tag{10}$$

where m is a parameter describing the roughness of the fracture-vug surface in the carbonate rock, $0 < m < 1$, and it describes the NF closure degree as a function of effective stress in the non-acid etching formation.

For the carbonate rocks with pores, fractures and vugs, its particle modulus is much higher than the bulk modulus. The volume change caused by the external stress is mainly the reduction of the volume of the pores, fractures, and vugs, and it is considered a decrease in porosity. The porosity as a function of the stress change is expressed as follows [27]:

$$\Delta\phi = \frac{\left(\nu + 2\nu^2 - 1\right)}{E(\nu - 1)}\Delta\sigma_1. \tag{11}$$

The boundary condition is expressed as follows:

$$F = \begin{cases} \left\{-\dfrac{\mathbf{n}^T}{n_w g \rho_w}\mathbf{k}\cdot\left(\dfrac{\partial p_w}{\partial x} - \rho_w g\right) - \bar{\mathbf{q}} = 0, \right. \\ p_w - \bar{p}_w = 0. \end{cases} \tag{12}$$

2.4. Criterion for Interaction between HF and NF. If NFs exist in carbonate rock, how the fractures propagate when the HF interacts with the NFs should be considered. When an HF intersects an NF, fracture crossing, diversion, arrest, and shear dilation occur. The interaction behavior is related to the geostress state, the mechanical properties of rock mass, the fluid rheology, and injection rate. Many scholars have put into theoretical and experimental research on HF-NF interaction, and the criteria for intersection have been proposed.

The approaching angle between the HF and the NF is denoted as β (Figure 2). According to Renshaw and Pollard's fracture crossing criterion, the NF is considered a friction interface, and the condition for no slippage along the friction interface is written as follows [26]:

$$\left|\tau_\beta\right| < S_0 - \lambda\sigma_{\beta y}, \tag{13}$$

$$\tau_\beta = K\sin\frac{\theta}{2}\sin\frac{3\theta}{2}\sin 2\beta + K\sin\frac{\theta}{2}\cos\frac{3\theta}{2}\cos 2\beta - \frac{\sigma_H - \sigma_h}{2}\sin 2\beta, \tag{14}$$

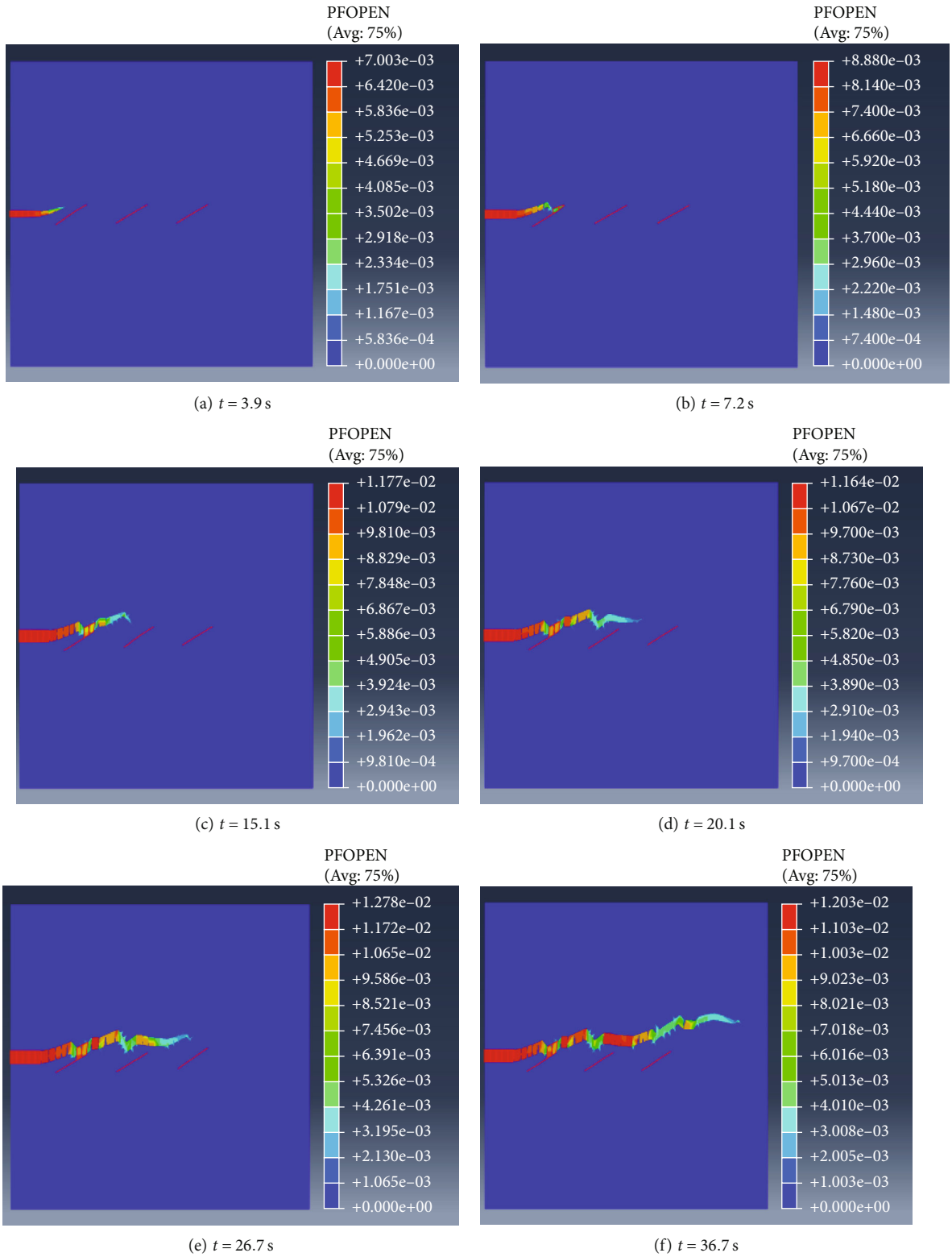

(a) $t = 3.9$ s (b) $t = 7.2$ s

(c) $t = 15.1$ s (d) $t = 20.1$ s

(e) $t = 26.7$ s (f) $t = 36.7$ s

Figure 23: HF propagation at the NF approaching angle of 45° and stress anisotropy coefficient of 0.2.

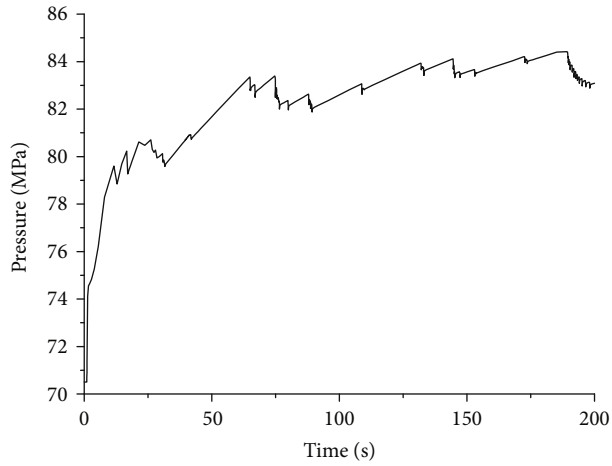

Figure 24: Pressure curve at the NF approaching angle of 45° and stress anisotropy coefficient of 0.2.

$$\sigma_{\beta y} = K + K \sin\frac{\theta}{2}\sin\frac{3\theta}{2}\cos 2\beta - K\sin\frac{\theta}{2}\cos\frac{3\theta}{2}\sin 2\beta + \frac{\sigma_H + \sigma_h}{2} - \frac{\sigma_H - \sigma_h}{2}\cos 2\beta, \tag{15}$$

$$\cos^2\frac{\theta}{2}K^2 + 2\left[\left(\frac{\sigma_H - \sigma_h}{2}\right)\sin\frac{\theta}{2}\sin\frac{3\theta}{2} - T\right]K + \left[T^2\left(\frac{\sigma_H - \sigma_h}{2}\right)^2\right] = 0, \tag{16}$$

where $\theta = \beta$ or $\beta - \pi$; $T = T_0 - [(\sigma_{\mathrm{H}} - \sigma_{\mathrm{h}})/2]$, and K is the solution of Equation (16) when $\sigma_1 = T_0$.

$$\begin{aligned}
\sigma_1 &= \frac{\sigma_x + \sigma_y}{2} + \sqrt{\left(\frac{\sigma_x - \sigma_y}{2}\right)^2 + \tau_{xy}^2},\\
\sigma_x &= \sigma_H + \frac{K_I}{\sqrt{2\pi r}}\cos\frac{\alpha}{2}\left(1 - \sin\frac{\alpha}{2}\sin\frac{3\alpha}{2}\right),\\
\sigma_y &= \sigma_h + \frac{K_I}{\sqrt{2\pi r}}\cos\frac{\alpha}{2}\left(1 + \sin\frac{\alpha}{2}\sin\frac{3\alpha}{2}\right),\\
\tau_{xy} &= \frac{K_I}{\sqrt{2\pi r}}\sin\frac{\alpha}{2}\cos\frac{\alpha}{2}\cos\frac{3\alpha}{2}.
\end{aligned} \tag{17}$$

2.5. Verification Example. To validate the reliability of the numerical FEM model, we compare the FEM solution with the analytical solution from the KGD model. The hydrofracture length and opening of the KGD model are as follows.

$$\begin{aligned}
L_{\mathrm{frac}}(t) &= 1.078\left(\frac{E' q_0^3}{\mu_f}\right)^{1/6} t^{2/3},\\
w_0^h(t) &= 2.36\left(\frac{\mu_f q_0^3}{E'}\right) t^{1/3},
\end{aligned} \tag{18}$$

where $E' = 2G/(1 - \nu)$. To reduce the computation load, we establish a symmetric FEM model. The model has a length of 100 m and a width of 120 m, and the model is gridded into 21,280 rectangular elements with pore pressure degree of freedom (i.e., CPE4P elements), the injection point at the center of the left boundary, pump rate per unit thickness as 0.12 m^3/min, bulk modulus of 2,200 MPa, shear modulus of 8,300 MPa, Poisson's ratio of 0.2, and fluid viscosity of 1 cp. A total of 133 COH2D4P cohesive elements are added along the central axis of the computation area, and the initial fracture width is 0.002 mm. The numerical solutions have a good agreement with the KGD analytical solution (Figure 3), which confirms the relative reliability of the FEM fracturing model.

3. Results and Analysis

3.1. Effects of Fluid Leakoff in Fracture and Vugs. In the acid fracturing process (Figure 4), the HF possibly intersects with fracture and vugs. The HF-NF interaction and vugs is simulated in Case 1: $C_L = 1 \times 10^{-12}$ m/(Pa · s) within 8 m from the wellbore, $C_L = 1 \times 10^{-8}$ m/(Pa · s) within 8-16 m, and $C_L = 1 \times 10^{-12}$ m/(Pa · s) beyond 16 m; Case 2: $C_L = 1 \times 10^{-8}$ m/(Pa · s) within 10 m and $C_L = 1 \times 10^{-12}$ m/(Pa · s) beyond 10 m; Case 3: $C_L = 1 \times 10^{-12}$ m/(Pa · s); and Case 4: $C_L = 1 \times 10^{-8}$ m/(Pa · s). Case 1 simulates that interconnection between the HF and the far field NF and vug. Case 2 simulates HF propagation after serious fluid leakoff in NFs and vugs only developed around the wellbore. Case 3 simulates HF propagation in the rock without NFs and vugs. Case 4 simulates HF propagation in the fractures and vugs both developed around the wellbore and in the far field. When the fluid flows into the vugs, fluid leakoff is increased. We use the equivalent method to perform FE modeling of the vugs in ABAQUS software. We write a subroutine program to represent the cavity in the finite element model, where the cavity has a large leakoff coefficient value. The results are as follows:

When the HF interacts with the vugs, HF is much difficult to propagate due to serious fluid leakoff and low net pressure in the HF (Figure 5). The pressure within the fracture during acid fracturing is shown in Figure 6. In Case 1, the HF is initiated from the wellbore and communicates with the fracture and vugs, the pressure rises slowly, and the HF breaks through the fracture-vug later. In Case 2, the pressure curve fluctuates,

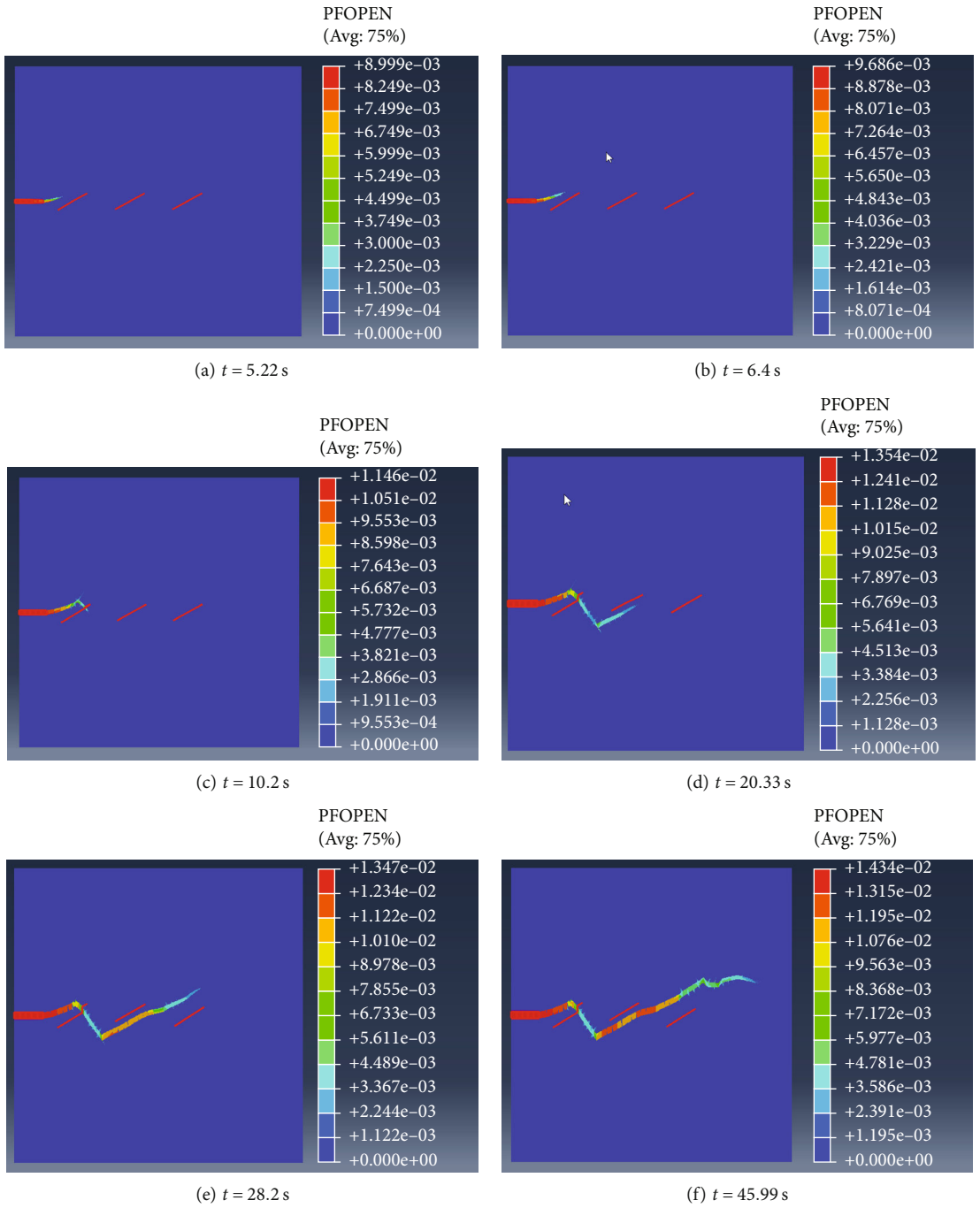

Figure 25: HF propagation at the NF approaching angle of 45° and stress anisotropy coefficient of 0.1.

reflecting balance between fluid leakoff and pressure build-up. In Case 3, the pressure is relatively stable, reflecting the typical characteristics of HF propagation. The pressure curve in Case 4 is similar to that in Case 2. When small pressure drop occurs during the HF interacts with the fracture-vug, it is suggested that the acid fracturing treatment should be operated by increasing the acid viscosity to reduce fluid leakoff, injecting fracturing fluid and acid fluid alternatively, increasing injection rate and injecting fibers and ceramics. When a large pressure drop occurs, it is suggested that the middle-low viscosity acid be injected at low rate to etch the carbonate rock and enhance the fracture conductivity.

The fracture pressure in Case 1 is close to that in Case 3 (Figure 7(a)), and the fracture propagates forward. The fracture pressure in Case 2 is close to that in Case 4 (Figures 7(b) and 7(c)).

3.2. Effects of Approaching Angles. The approaching angle is set as 0°-30° , 30°-60°, and 60°-90°, respectively, and the effects of approaching angles on HF propagation are simulated.

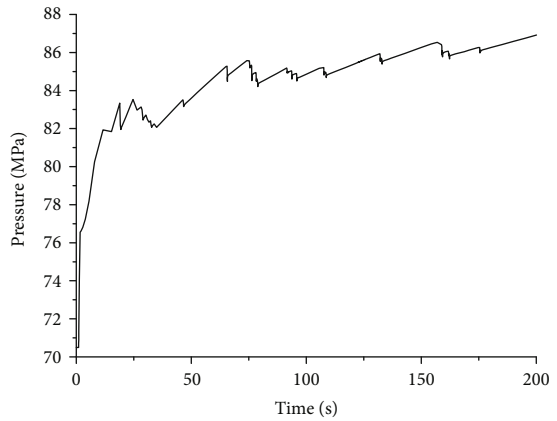

Figure 26: Pressure curve at the NF approaching angle of 45° and stress anisotropy coefficient of 0.1.

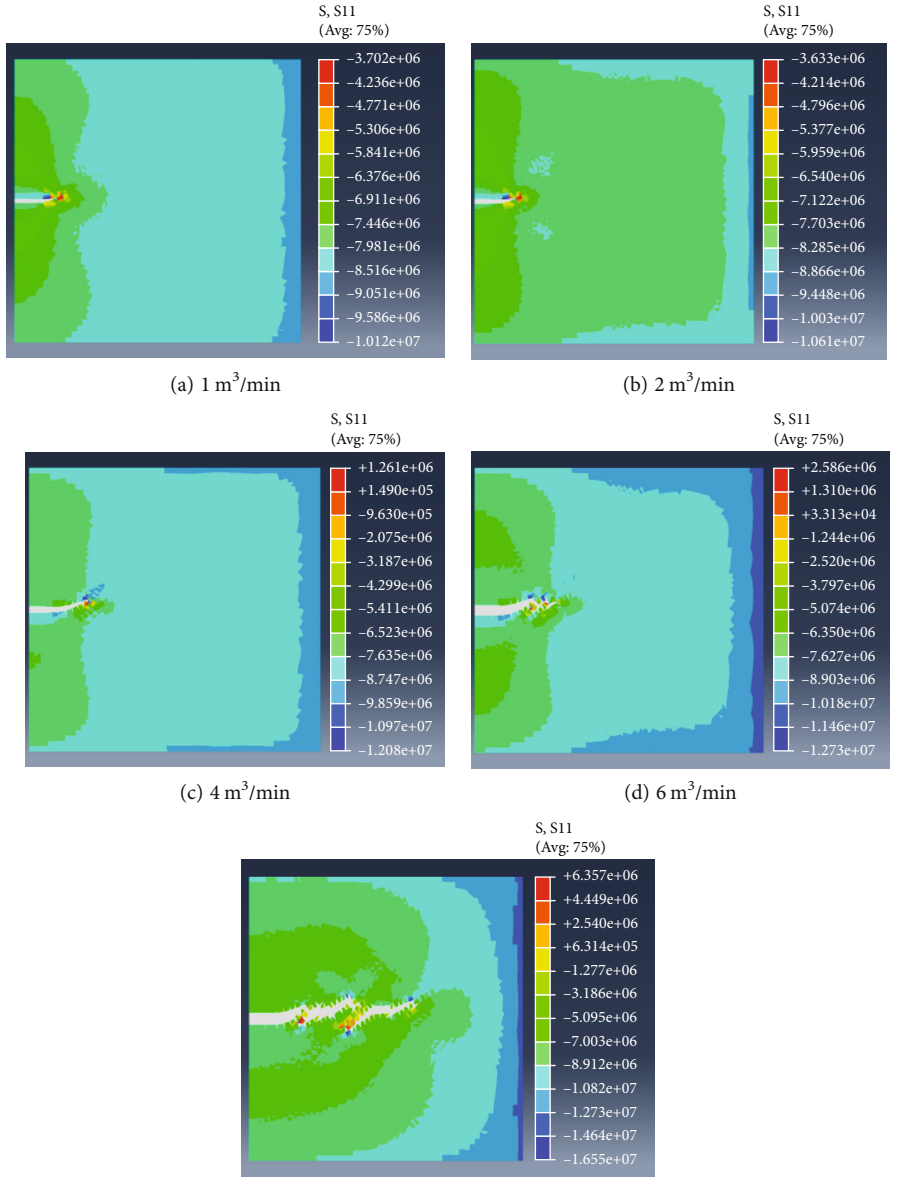

(a) 1 m^3/min

(b) 2 m^3/min

(c) 4 m^3/min

(d) 6 m^3/min

(e) 8 m^3/min

Figure 27: Contour map of stress S_{11} at the NF approaching angle of 45° and at the rate of 1-8 m^3/min.

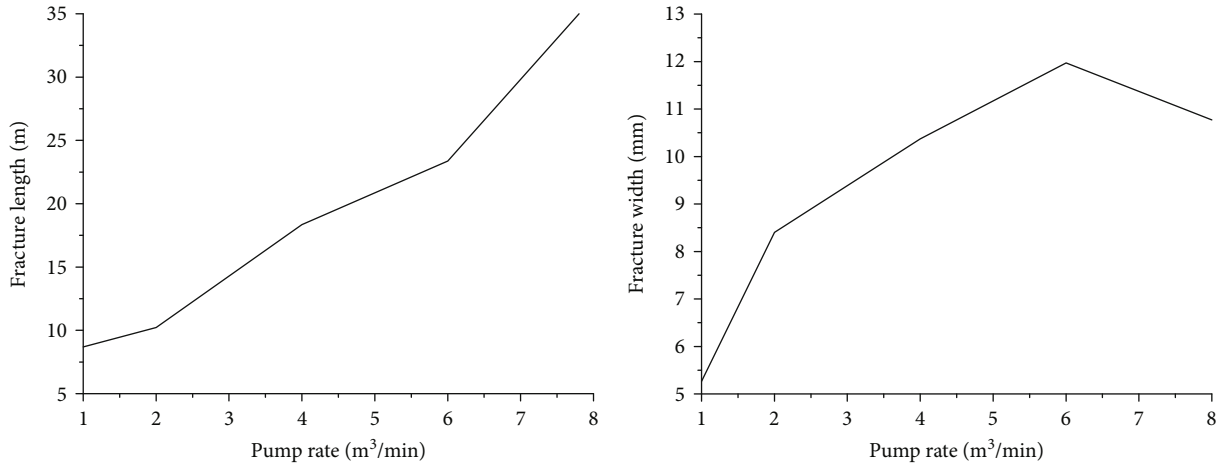

(a) Fracture length (b) Fracture width

Figure 28: Fracture length and width at the NF approaching angle of 45° and at the rate of 1-8 m³/min.

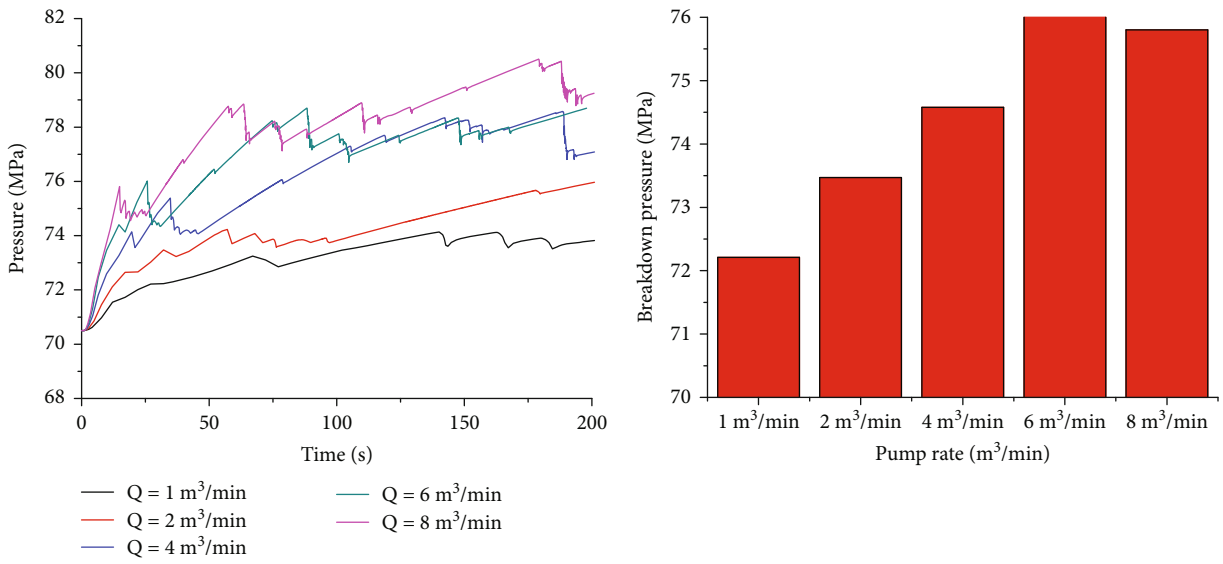

(a) Pressure within the fracture (b) breakdown pressure

Figure 29: Pressure within the fracture and fracture pressure at the NF approaching angle of 45° and at the injection rate of 1-8 m³/min.

3.2.1. Interaction between the HF and NFs at Approaching Angles of 0°-30°

(1) Establishment of FE Model. We establish the physical model of three NFs intersected with one HF in the carbonate reservoir (Figure 8) and perform model meshing with the unstructured grid elements, including 3,014 quadrilateral solid elements, 5,928 HF elements, and 15,167 nodes. The parameters are listed in Table 1. Numerical simulation on HF propagation at the approaching angle of 30° and various principal stress difference is carried out.

(2) Effect of Stress Difference on Multi-HF Propagation. When the stress anisotropy coefficient is 0.3, the HF is diverted upward before intersecting with the NF1 (Figure 9(a)), and then, the HF propagates upward and it still does not intersect with NF1 (Figure 9(b)), and the HF does not intersect with NF2 and is diverted upward (Figures 9(c) and 9(d)). The pressure curve shows the fluctuation and oscillation characteristics (Figure 10). When the HF meets with the NF, the HF is diverted, and fluid leakoff and HF propagation are in balance.

When the stress anisotropy coefficient is 0.3, the HF is diverted upward before intersecting with the NF1 (Figure 11(a)), and then, the HF does not intersect with NF1 (Figure 11(b)), and the HF does not intersect with NF2 and is diverted upward (Figures 11(c) and 11(d)). The pressure curve shows the fluctuation and oscillation characteristics (Figure 12).

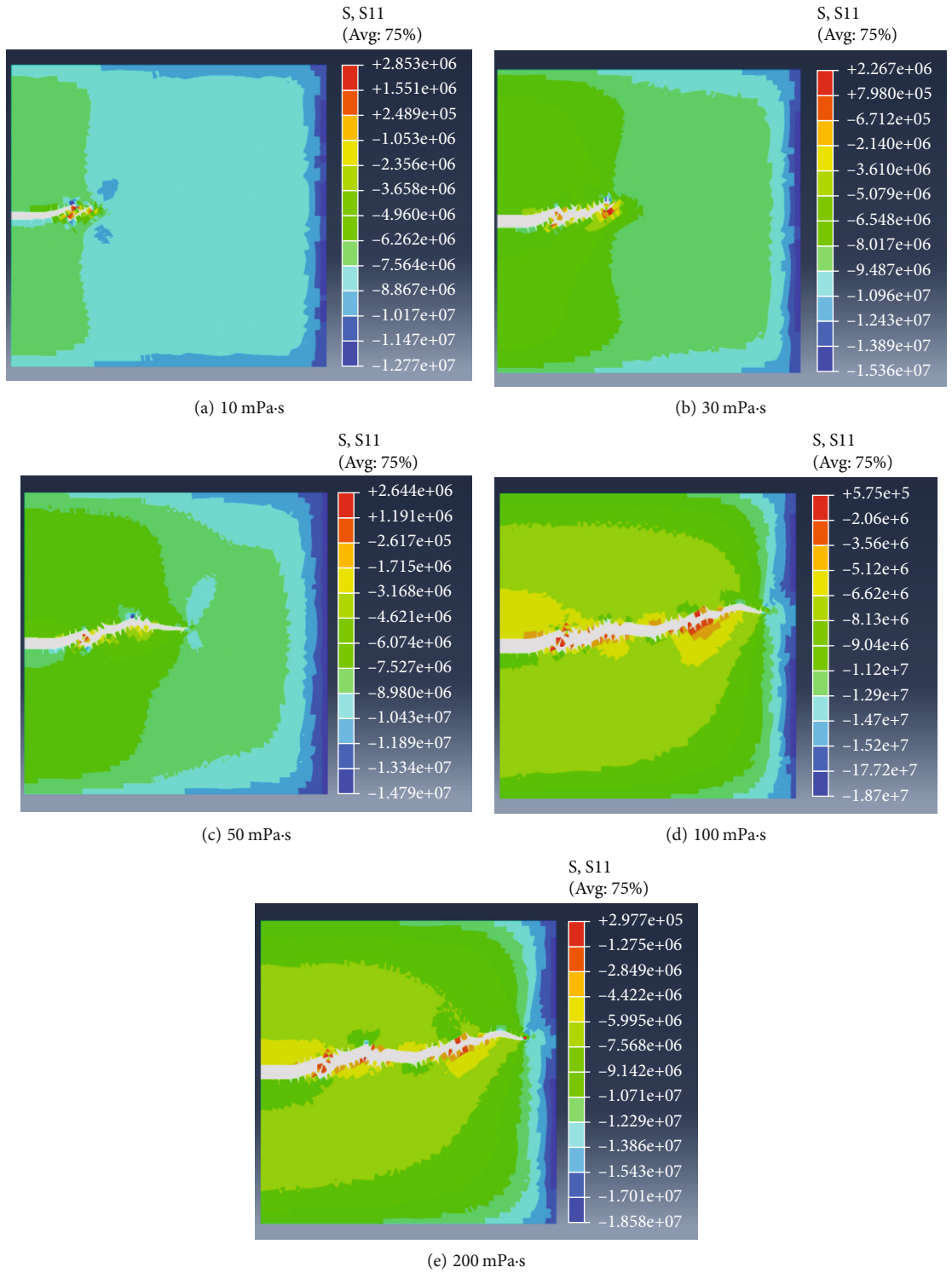

(a) 10 mPa·s

(b) 30 mPa·s

(c) 50 mPa·s

(d) 100 mPa·s

(e) 200 mPa·s

Figure 30: Stress contour map at the NF approaching angle of 45° and under fluid viscosity of 10-200 mPa·s.

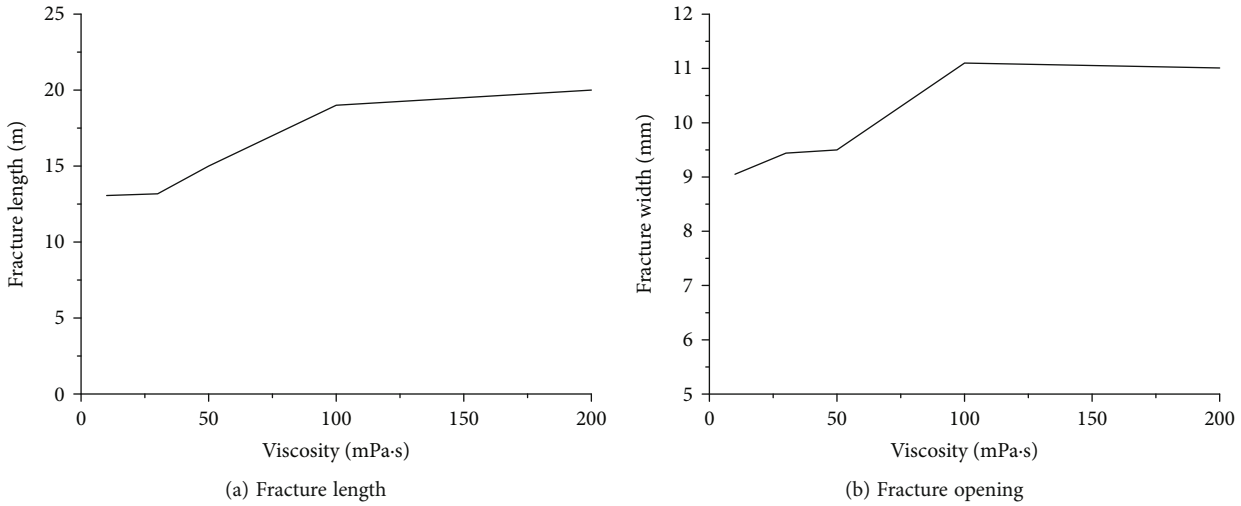

(a) Fracture length (b) Fracture opening

Figure 31: Fracture length and width at the NF approaching angle of 45° and under fluid viscosity of 10-200 mPa·s.

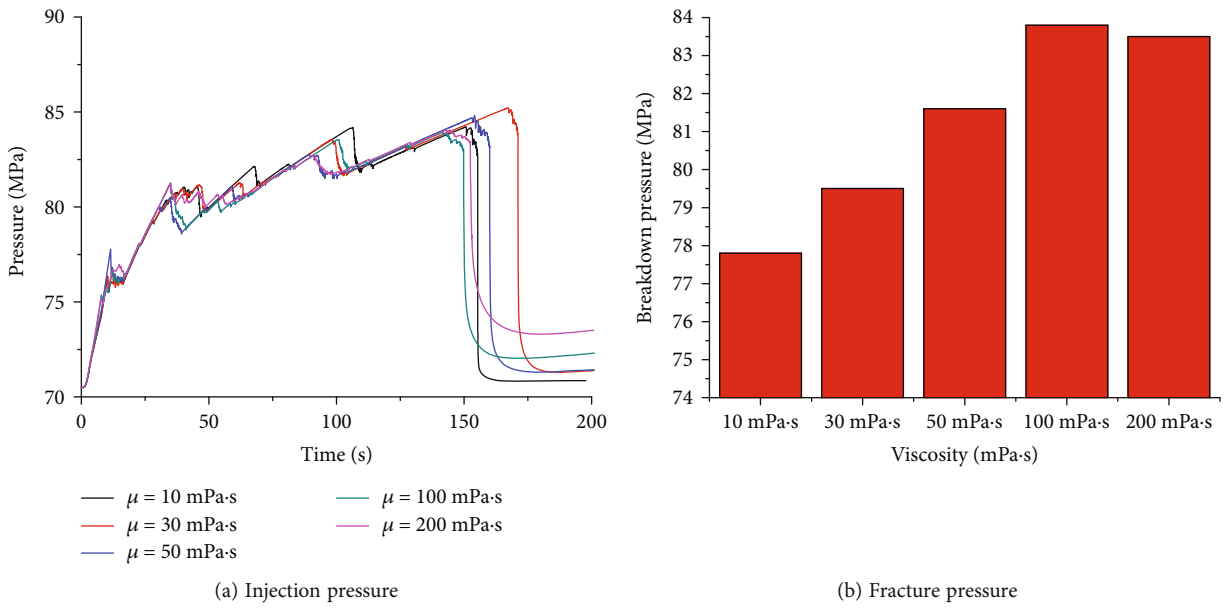

(a) Injection pressure (b) Fracture pressure

Figure 32: Injection pressure and fracture pressure at the NF approaching angle of 45° and under fluid viscosity of 10-200 mPa·s.

When the stress difference coefficient is 0.1, the HF is diverted upward before intersecting with the NF1 (Figure 13(a)), and then, the HF does not intersect with NF1 (Figure 13(b)), and the HF does not intersect with NF2 and is diverted upward (Figures 13(c) and 13(d)). The injection pressure shows a fluctuation charateristic during fracking treatment (Figure 14).

(3) Impacts of Injection Rate on HF Propagation. HF propagation during acid fracturing at different injection rates of 1 m^3/min, 2 m^3/min, 4 m^3/min, 6 m^3/min, and 8 m^3/min is simulated (Figure 15), and the longer fracture is created at higher injection rate. It is recommended to carry out acid fracturing with the highest injection rate possible so that the HFs communicate with the fractures and vugs.

A higher injection rate is required to make HF cross the NF. When the injection rate reaches 6 m^3/min, increment of fracture length and width slows down (Figure 16), and the optimal injection rate is 6 m^3/min.

The pressures within the fracture and breakdown pressure are shown in Figure 17. We identify the breakdown pressure where the point on the injection pressure has a large pressure drop at the initial stage of fracking. When the injection rate is

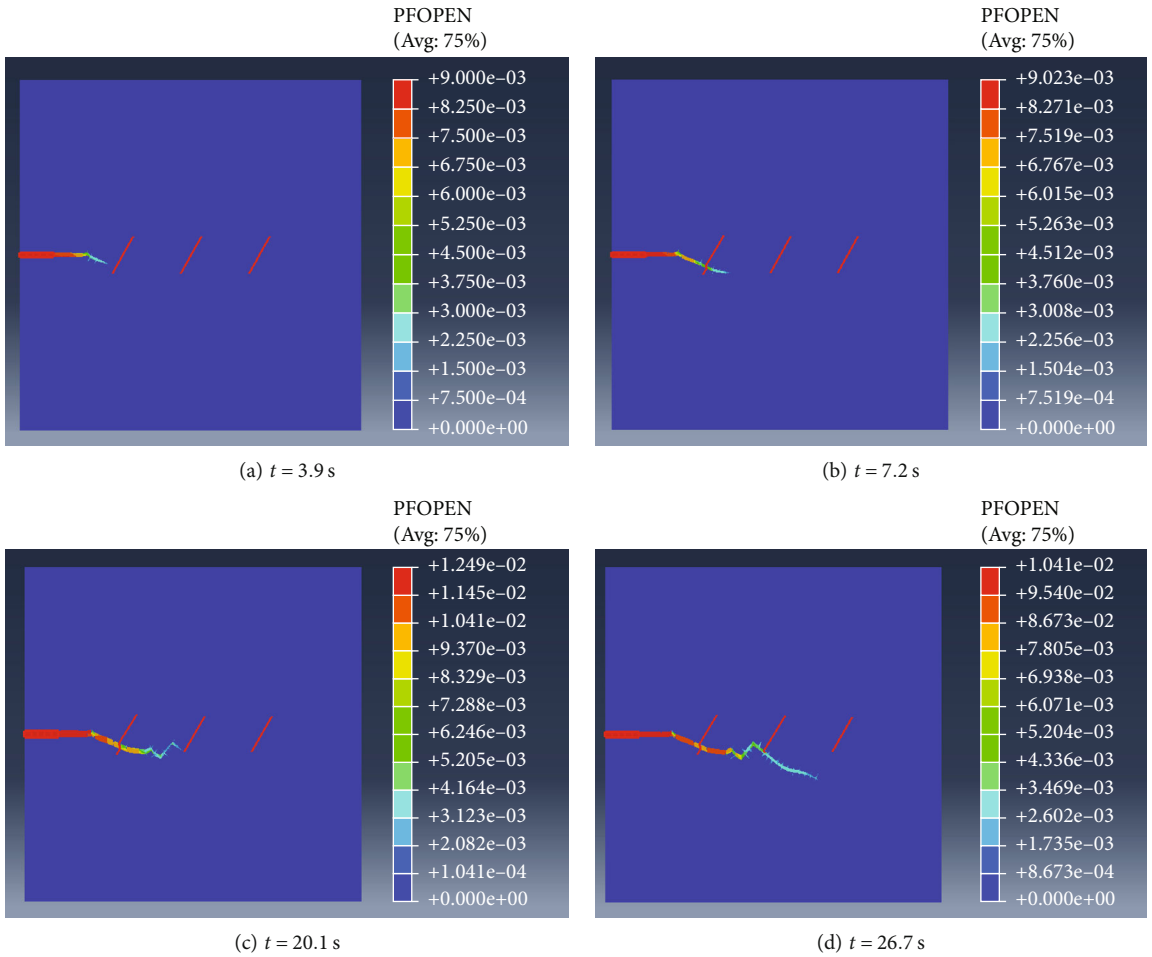

Figure 33: HF propagation at the NF approaching angle of 60° and under stress anisotropy coefficient of 0.3.

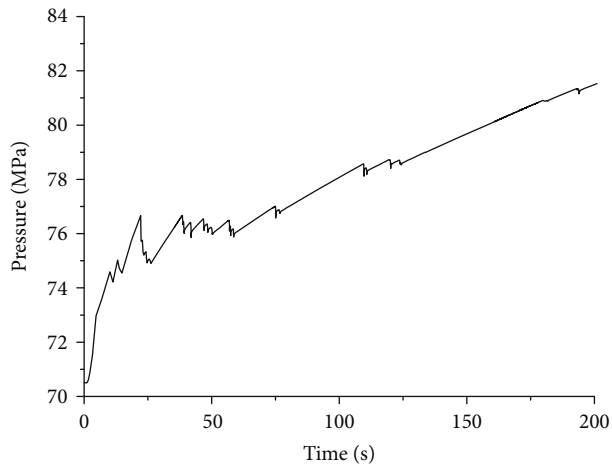

Figure 34: Pressure curve at the NF approaching angle of 60° and under stress anisotropy coefficient of 0.3.

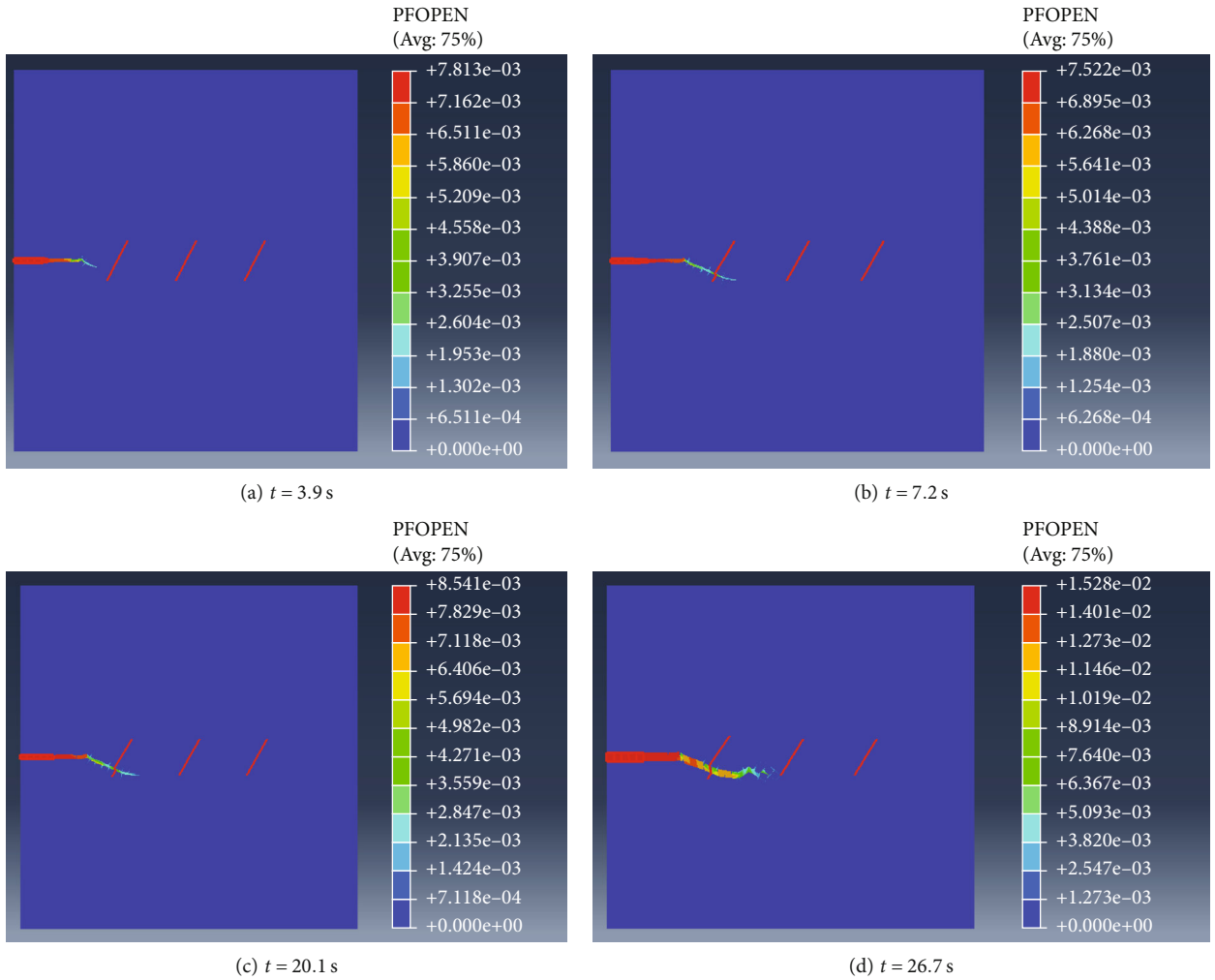

Figure 35: HF propagation at the NF approaching angle of 60° and under a stress anisotropy coefficient of 0.2.

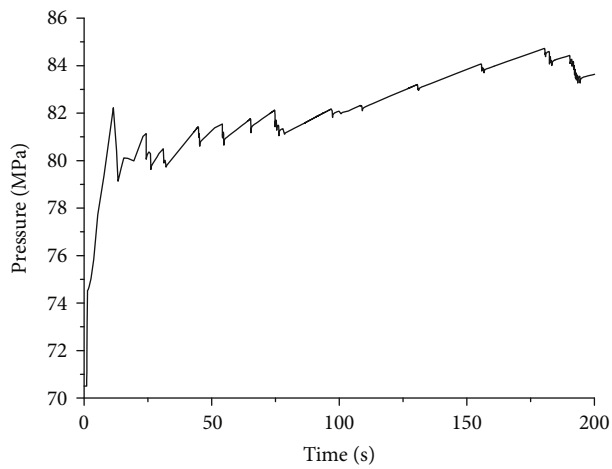

Figure 36: Pressure curve at the NF approaching angle of 60° and under a stress anisotropy coefficient of 0.2.

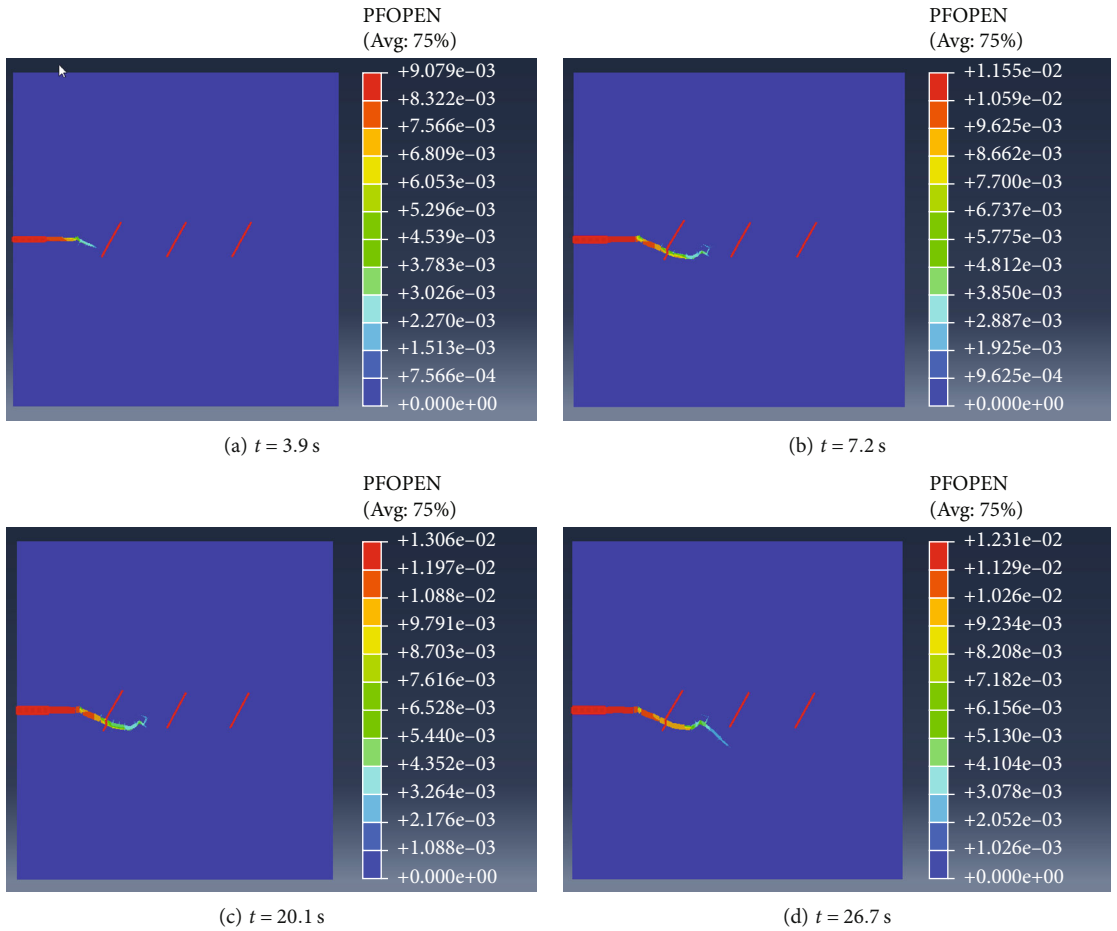

(a) $t = 3.9$ s (b) $t = 7.2$ s

(c) $t = 20.1$ s (d) $t = 26.7$ s

Figure 37: HF propagation at the NF approaching angle of 60° and under the stress anisotropy coefficient of 0.1.

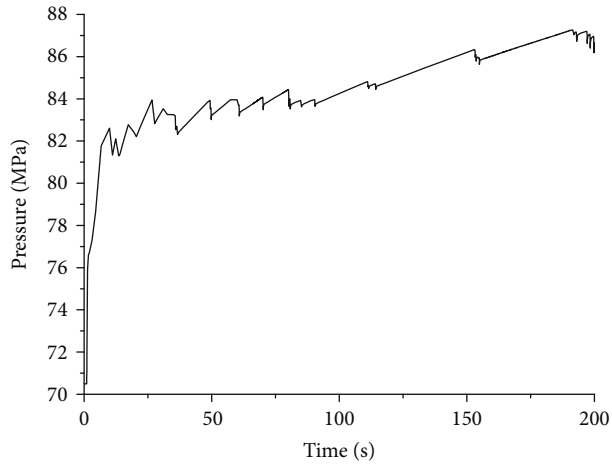

Figure 38: Pressure curve at the NF approaching angle of 60° and under a stress anisotropy coefficient of 0.1.

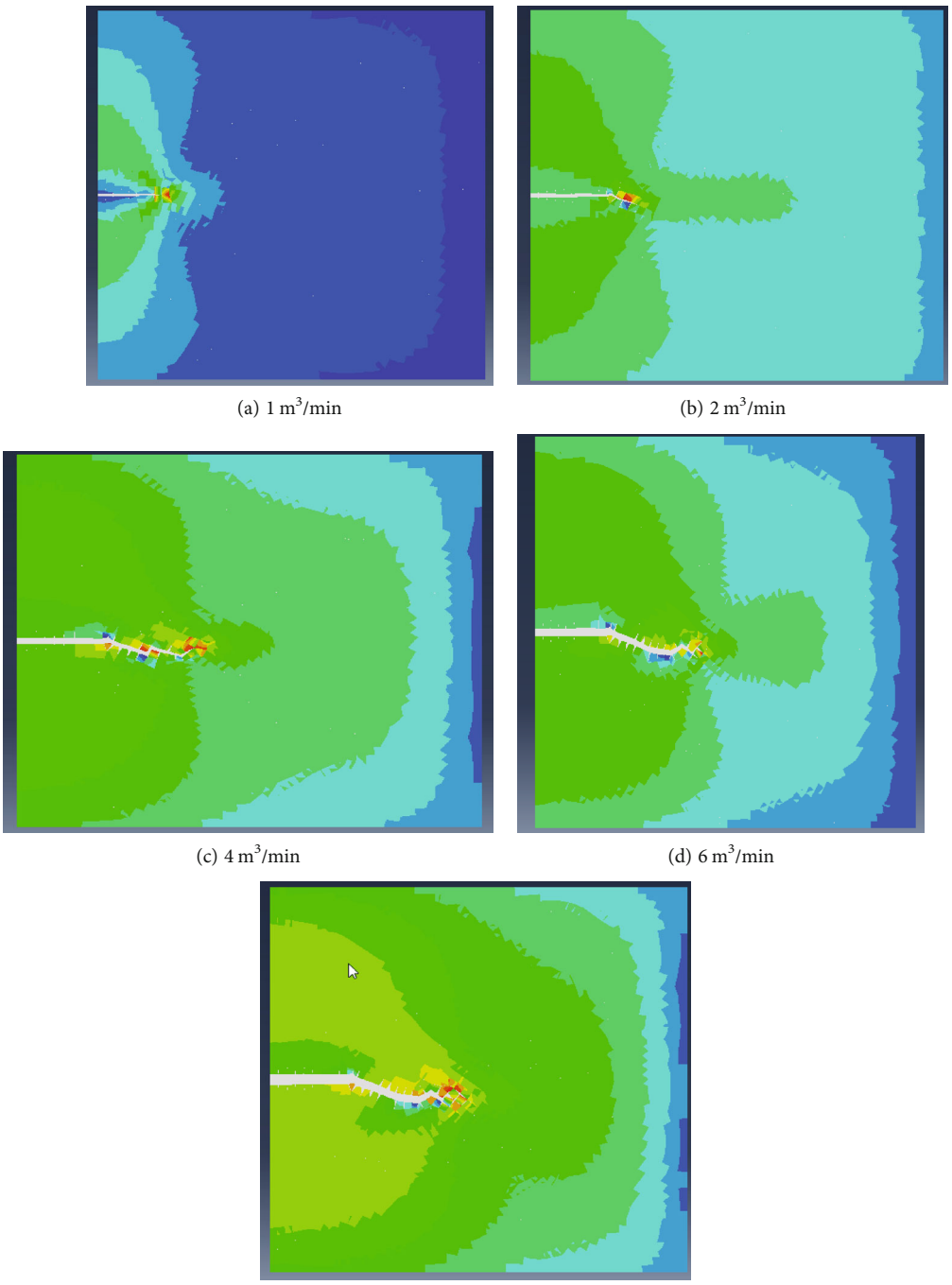

(a) 1 m^3/min (b) 2 m^3/min

(c) 4 m^3/min (d) 6 m^3/min

(e) 8 m^3/min

Figure 39: Contour map of stress S_{11} at the NF approaching angle of 60° and pump rates of 1-8 m^3/min.

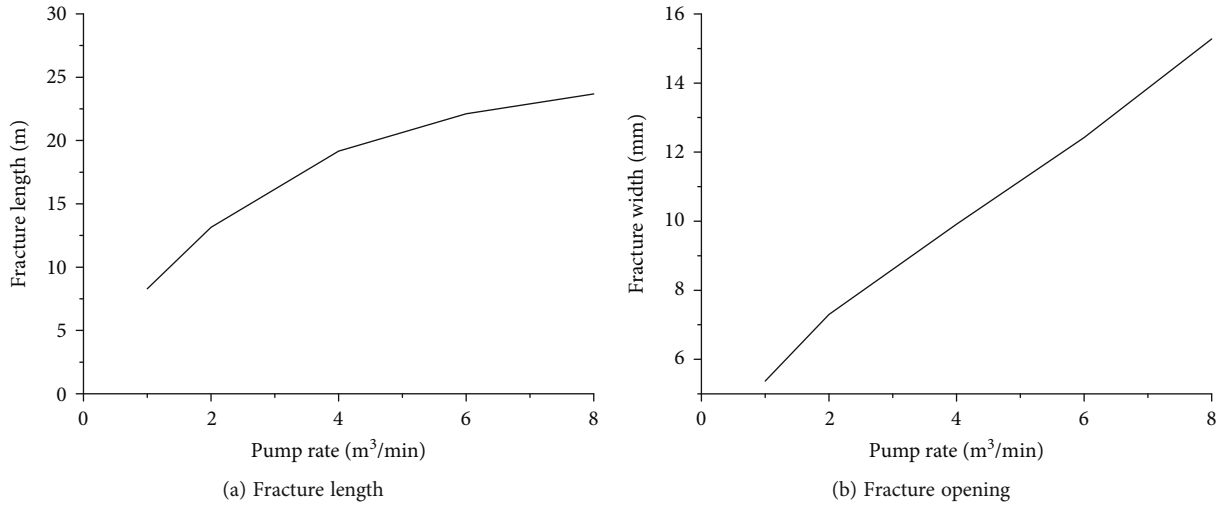

(a) Fracture length (b) Fracture opening

FIGURE 40: Fracture length and width at the NF approaching angle of 60° and injection rates of 1-8 m³/min.

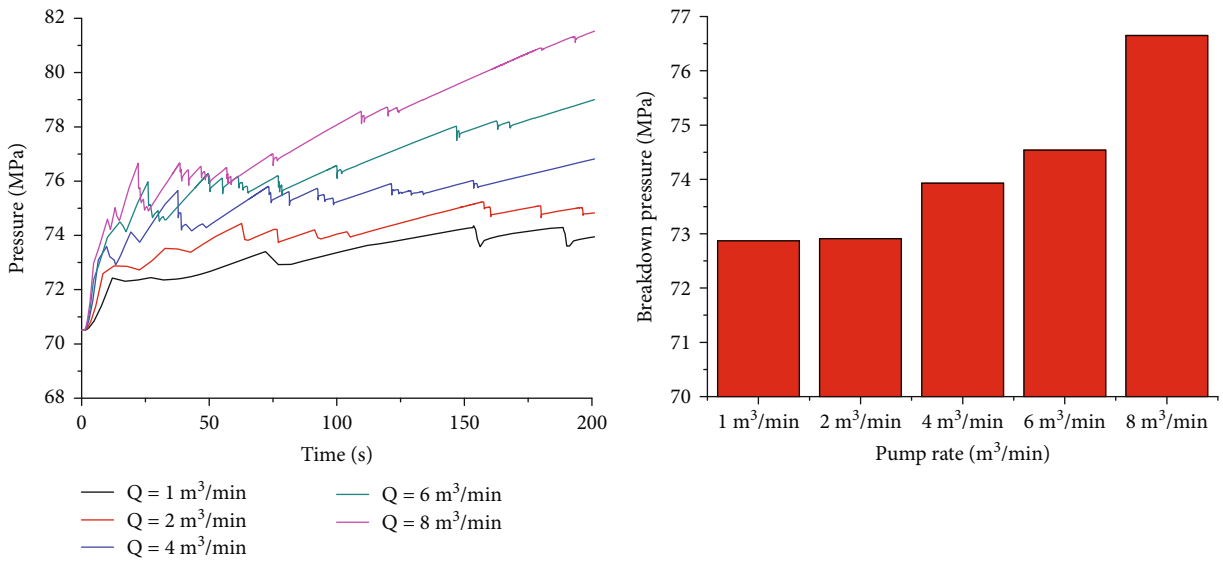

(a) Pressure within the fracture (b) Fracture pressure

FIGURE 41: Pressure within the fracture and fracture pressure at the NF approaching angle of 60° and injection rates of 1-8 m³/min.

low, the HF is difficult to communicate with NF1 due to serious acid loss and low net pressure. When the injection rate is high, obvious fracture points occur and the pressure curves show the jagged fluctuation, and the HF tends to communicate with the fracture and vugs. Breakdown pressure does not increase obviously with the injection rate due to NF development.

(4) Effects of Fluid Viscosity on HF Propagation. HF propagation in acid fracturing under the acid viscosity of 10 mPa·s, 30 mPa·s, 50 mPa·s, 100 mPa·s, and 200 mPa·s is simulated (Figure 18), and the longer fracture is created under higher fluid viscosity. Increment of fracture length and width slows down when the fluid viscosity reaches 50 mPa·s (Figure 19). The optimal fluid viscosity is about 50 mPa·s.

When the viscosity is low, serious fluid leakoff occurs, and the net pressure in the fracture is low. The HF is difficult to communicate with NF1 (Figure 20). When the viscosity is higher, there are multiple fracture points, the pressure curves show the characteristics of jagged fluctuation, and the HF tends to communicate with the NFs and vugs. The pressure curve under the fluid viscosity of 50 mPa·s is similar to that under the fluid viscosity of 100 mPa·s. Due to the existence of NFs, the fracture pressure does not increase significantly

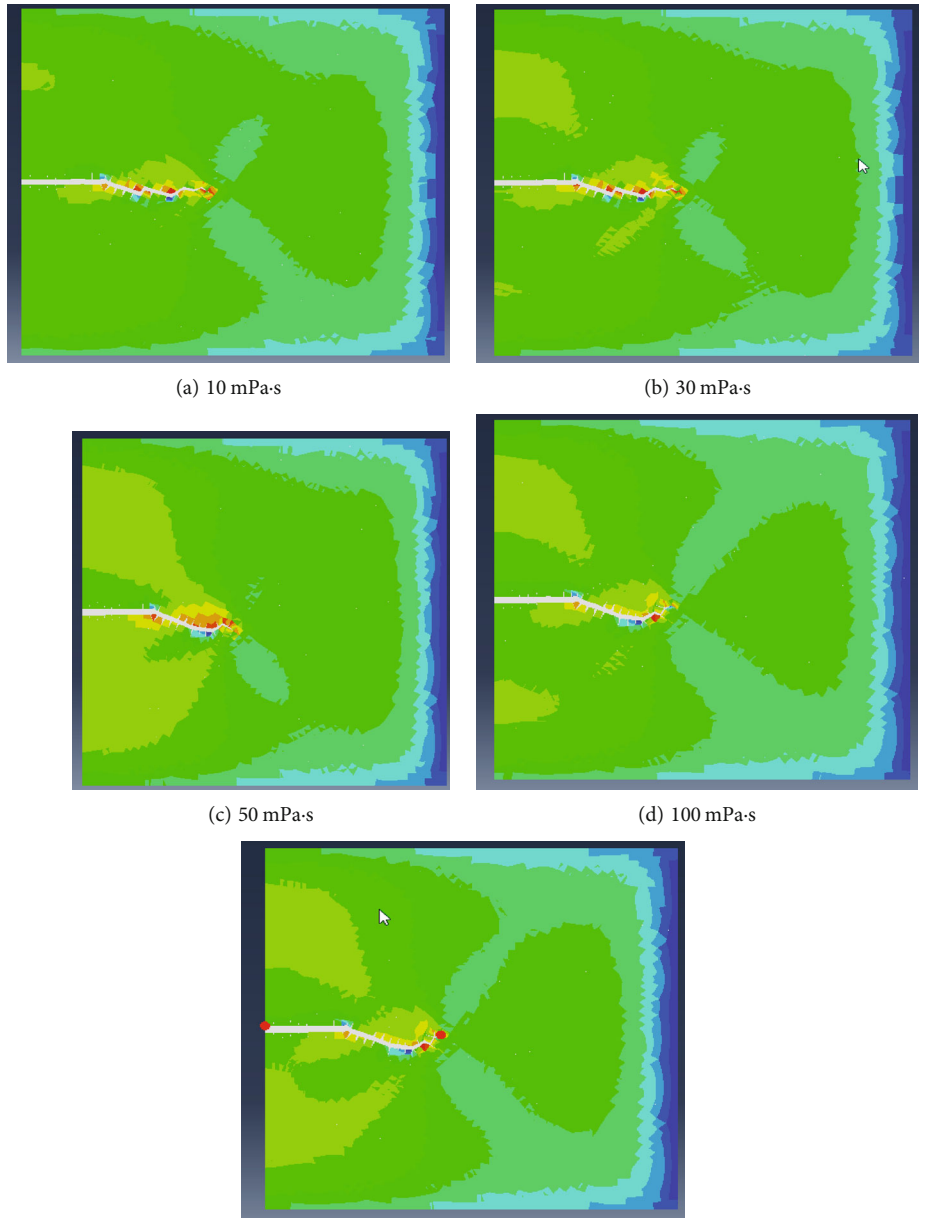

(a) 10 mPa·s (b) 30 mPa·s

(c) 50 mPa·s (d) 100 mPa·s

(e) 200 mPa·s

Figure 42: Stress contour map at the NF approaching angle of 60° and under the acid viscosity of 10-200 mPa·s.

with the viscosity, and the fracture pressure increases step by step, requiring a higher net pressure to communicate with the fracture-vug.

3.2.2. Interaction between the HF and NFs at Approaching Angles of 30°-60°

(1) Effect of Stress Difference. Interaction of HFs and NFs at the approaching angle of 45° and under a stress anisotropy coefficient of 0.3 is simulated (Figure 21). When injection time $t = 3.9$ s, the HF is diverted upward before intersecting with NF1. When $t = 6.5$ s, the HF intersects with NF1 and propagates upward along the right side of NF1. When $t = 17.5$ s, the HF is diverted toward NF2. When $t = 22.3$ s, the HF intersects NF2. When $t = 28.2$ s, the HF is diverted toward NF3. When $t = 36.7$ s, the HF bypasses NF3.

The pressure curve exhibits obvious oscillation characteristics, indicating interaction between HFs and NFs, HF diversion, and balance between fluid leakoff and fracture propagation (Figure 22). When the HF encounters the NF, the breakdown pressure gradually increases. When the HF intersects with NF1, the breakdown pressure drops rapidly. When the HF intersects with NF2, the breakdown pressure drops rapidly. Then, the HF is diverted toward the NF firstly and bypasses the NF then, and the breakdown pressure in the fracture gradually rises.

Interaction of HFs and NFs at the approaching angle of 45° and under a stress anisotropy coefficient of 0.2 is simulated

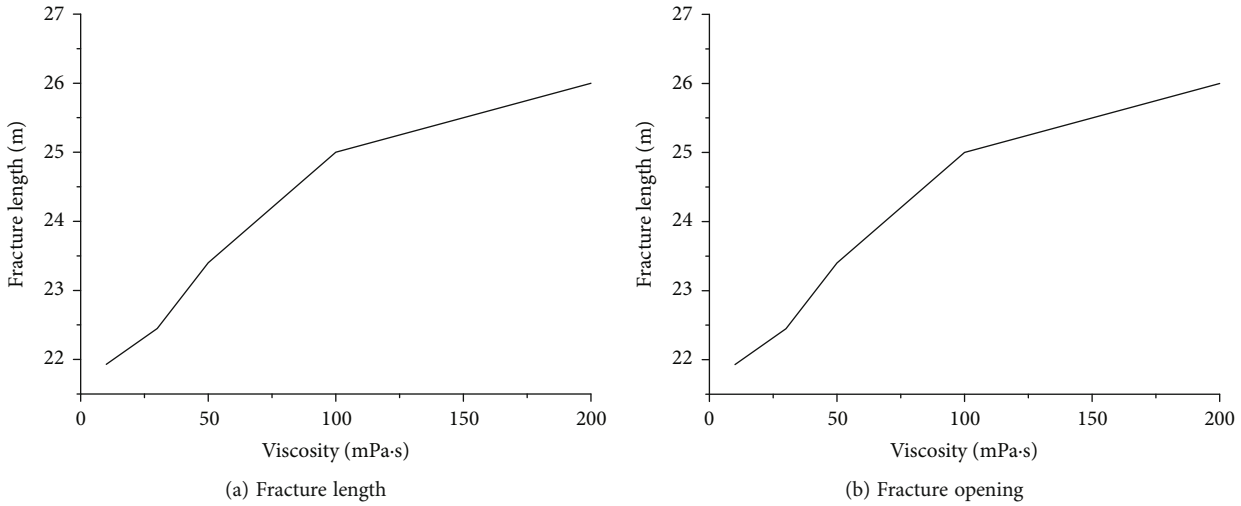

(a) Fracture length (b) Fracture opening

Figure 43: Fracture length and width at the NF approaching angle of 60° and under the acid viscosity of 10-200 mPa·s.

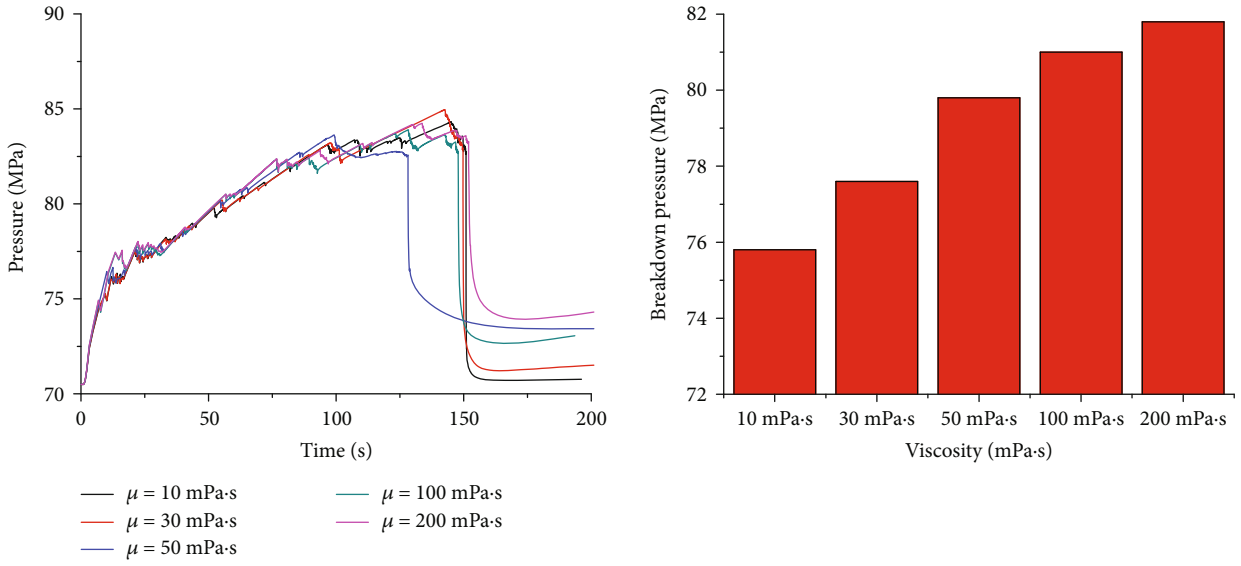

Figure 44: Injection pressure and fracture pressure at the NF approaching angle of 60° and under the acid viscosity of 10-200 mPa·s.

(Figure 23). When $t = 3.9$ s, the HF is diverted upward before intersecting NF1. When $t = 7.2$ s, the HF intersects with NF1 and propagates upward along the right side of NF1. When $t = 15.1$ s, the HF is diverted toward NF2. When $t = 20.1$ s, the HF is diverted downward and bypasses NF2. When $t = 26.7$ s, the HF is diverted toward NF3. When $t = 37.1$ s, the HF bypasses NF3.

The pressure curve exhibits obvious oscillation characteristics, indicating interaction between HFs and NFs, HF diversion, and balance between fluid leakoff and fracture propagation (Figure 24). When the HF encounters the NF, the breakdown pressure gradually increases. When the HF intersects with NF1, the breakdown pressure drops rapidly. Then, the HF is diverted toward the NF firstly and bypasses the NF, and the breakdown pressure in the fracture gradually rises.

Interaction of HFs and NFs at the approaching angle of 45° and under a stress anisotropy coefficient of 0.1 is simulated (Figure 25). When $t = 5.22$ s, the HF is diverted upward before intersecting NF1. When $t = 6.4$ s, the HF does not intersect with NF1 and propagates upward along the right side of NF1. When $t = 10.2$ s, the HF is diverted toward NF2. When $t = 20.33$ s, the HF is diverted downward and bypasses NF2. When $t = 26.7$ s, the HF is diverted toward NF3. When $t = 45.99$ s, the HF bypasses NF3.

The pressure curve exhibits obvious oscillation characteristics as illustrated above, indicating an interaction between HFs and NFs, HF diversion, and balance between fluid leakoff and fracture propagation (Figure 26).

(2) Effects of Injection Rate. HF propagation in acid fracturing and at the acid injection rates of 1-8 m^3/min is simulated (Figure 27), and the longer fracture is created at a higher injection rate. The optimal injection rate is also 6 m^3/min (Figure 28).

The pressure within the fracture and breakdown pressure at the NF approaching angle of 45° and at the rate of 1-8 m^3/min (Figure 29) shows characteristics similar to those at the NF approaching angle of 30°.

(3) Effects of Fluid Viscosity. HF propagation in acid fracturing at the NF approaching angle of 45° and under the acid viscosity of 10 mPa·s, 30 mPa·s, 50 mPa·s, 100 mPa·s, and 200 mPa·s is simulated (Figure 30). The optimal fluid viscosity is about 50 mPa·s (Figure 31).

When the viscosity is low, serious fluid leakoff occurs, and the net pressure in the fracture is low. The HF is difficult to communicate with NF1. When the viscosity is higher, there are multiple fracture points, the pressure curves show the characteristics of jagged fluctuation, and the HF tends to communicate with the fractures and vugs. The pressure curve under the fluid viscosity of 50 mPa·s is similar to that under the fluid viscosity of 100 mPa·s. Due to the existence of NFs, the breakdown pressure does not increase significantly with the viscosity, and the breakdown pressure increases step by step, requiring a higher net pressure to communicate with the fracture-vug (Figure 32).

3.2.3. Interaction between the HF and Multiple NFs with Angles of 60°

(1) Effect of Stress Difference. Interaction of HFs and NFs at the approaching angle of 60° and under a stress anisotropy coefficient of 0.3 is simulated (Figure 33). The HF is diverted downward before intersecting NF1. Then, the HF intersects with NF1 and propagates upward along the right side of NF1. Finally, the HF intersects NF2. The pressure curve exhibits obvious oscillation, indicating interaction between HFs and NFs, HF diversion, and balance between fluid leakoff and fracture propagation (Figure 34).

Interaction of HFs and NFs at the approaching angle of 60° and under a stress anisotropy coefficient of 0.2 is simulated (Figure 35). Firstly, the HF is diverted downward before intersecting NF1. Then, the HF intersects with NF1 and propagates upward along the right side of NF1. Finally, the HF intersects NF2. The pressure curve exhibits obvious oscillation characteristics as illustrated above (Figure 36).

Interaction of HFs and NFs at the approaching angle of 60° and under a stress anisotropy coefficient of 0.1 is simulated (Figure 37). HF propagation and pressure curves show the characteristics similar to those under a stress anisotropy coefficient of 0.3 and 0.2 (Figure 38).

(2) Effects of Injection Rate. HF propagation in acid fracturing at the acid injection rates of 1-8 m^3/min is simulated (Figure 39), and the optimal injection rate is 6 m^3/min (Figure 40).

When the injection rate is low, the HF is difficult to communicate with NF1 due to serious acid loss and low net pressure, and breakdown pressure does not increase significantly due to the existence of NFs (Figure 41).

(3) Effects of Fluid Viscosity. HF propagation in acid fracturing at the NF approaching angle of 60° and under the acid viscosity of 10-200 mPa·s is simulated (Figure 42). The optimal fluid viscosity is about 100 mPa·s (Figure 43).

When the viscosity is low, serious fluid leakoff occurs, and the net pressure in the fracture is low. The HF is difficult to communicate with NF1. When the viscosity is higher, there are lymultiple fracture points, the pressure curves show the characteristics of jagged fluctuation, and the HF tends to communicate with the fractures and vugs. The pressure curve under the fluid viscosity of 100 mPa·s is similar to that under the fluid viscosity of 200 mPa·s. Due to the existence of NFs, the breakdown pressure does not increase significantly with the viscosity, and the breakdown pressure increases step by step, requiring a higher net pressure to communicate with the fracture-vug (Figure 44).

4. Conclusions

We use the equivalent method of reducing rock strength by acid etching and serious fluid leakoff during the interaction of HFs and vug to establish a FE model of HF propagation during acid fracturing in fractured-vuggy carbonate formations. The effects of serious fluid leakoff in the fracture and vugs and reservoir properties on HF propagation during acid fracturing are simulated. The conclusions are as follows:

(1) We establish the FE model to simulate the effect of injection rate and fluid viscosity on HF propagation in acid fracturing in the carbonate rock and analyze the fracture characteristics of carbonate rock under different injection parameters. The optimal pump rate is 6 m^3/min, and the optimal viscosity is 100 mPa·s

(2) In the case of high breakdown pressure, it is recommended to inject the acid at a low rate (<2 m^3/min), and acid solution increases fluid leakoff to reduce breakdown pressure, and inject the acid at a high rate (>6 m^3/min) to reduce fluid leakoff

(3) If there is a low pressure drop, it is recommended to increase the crosslinking strength of the acid liquid or increase the injection rate and inject the fiber and proppant to reduce the fluid leakoff. The fracturing fluid and the acid solution are injected alternatively. If there is a large pressure drop, it is recommended to inject the medium and low viscosity acid solution at a low rate to etch the fracture and increase the fracture conductivity

(4) The intersection characteristics of HFs and NFs and the variation characteristics of bottom-hole pressure under different approaching angles are clarified. HF propagation requires higher pressure when the approaching angle is smaller

(5) We clarify characteristics of HFs communicating with NFs under different horizontal stress anisotropy coefficients. With the increase in stress anisotropy

coefficient of 0-30° approaching angle reservoir and 30-60° approaching angle reservoir, the shear stress of NFs increases, HFs are easy to open NFs, and the extension pressure of HFs decreases. The normal stress of the fracture increases, the HF is difficult to open the NF, and the extension pressure of the HF increases

(6) Interaction between HFs and multiple NFs under different injection parameters is analyzed. HF propagation in acid fracturing at different injection rates and viscosities is analyzed. The optimal injection rate is 8 m^3/min and the optimal viscosity is 50 mPa·s

(7) This paper provides a novel fracture propagation model in acid fracturing of carbonate reservoirs, which assumes that the fracture surface is smooth. However, rough fractures are often generated in acid fracturing process because the chemical reaction between the fracture wall and acid fluid. Therefore, fracture roughness should be considered as our next work in future.

Nomenclature

w: Fracture width
p: Fluid pressure in the fracture
q_l: Carter leakoff rate
c_l: Fracturing fluid leakoff coefficient
t: Fracturing operation time
$\tau(x)$: Initial fluid leakoff time at the position x
x: Location at the fracture
μ: Fracturing fluid viscosity
Q: Fracturing rate
n: Outward unit normal vector on the fracture
p: Fluid pressure
G: Rock shear modulus
ν: Poisson's ratio
$\sigma_{\min}$: Minimum closurestress
T: Net pressure within the fracture
σ_{ij}: Stress component
α: Biot coefficient
f_i: Body force component
$k(\sigma_e)$: Permeability
σ_e: Effective stress
C: Compressibility
$\varphi(\sigma_e)$: Porosity
λ: Friction coefficient at the NF surface
S_0: Cohesion force of the NF surface
τ_β: Shear stress on the NF surface
$\sigma_{\beta y}$: Normal stress on the NF surface
β: Angle between the NF and the HF
σ_H: Maximum horizontal principal stresses
σ_h: Minimum horizontal principal stress
T_0: Rock tensile strength
K_I: Type I stress intensity factor at the fracture tip
r: Polar coordinate at the fracture tip
α: Polar coordinate at the fracture tip
σ_x: Stress component x
σ_y: Stress component y
τ_{xy}: Shear stress component
t: Injection duration
q_0: Fracturing rate
μ_f: Fracturing fluid viscosity
E': Planar modulus
G: Shear modulus of rock.

Data Availability

Datasets related to this article can be found by connecting the corresponding authors.

Conflicts of Interest

The authors declare that they have no conflict of interests.

Acknowledgments

This work was supported financially by the Basic Research Program on Deep Petroleum Resource Accumulation and Key Engineering Technologies (No. U19B6003), the Open Fund of State Key Laboratory of Shale Oil and Gas Enrichment Mechanisms and Effective Development (No. 35800000-22-ZC0607-0021), the National Natural Science Foundation of China (No. 51936001 and No. 52274002), the Beijing Natural Science Foundation Project (No. 3222030), and the PetroChina Science and Technology Innovation Foundation Project (No. 2021DQ02-0201).

References

[1] B. Guan, C. Zhang, S. Li et al., "Three-stage reservoir unit description and benefit development of fracture controlled cave carbonate reservoirs in Tazhong Uplift, Tarim Basin," *Natural Gas Geoscience*, vol. 31, pp. 1766–1778, 2020.

[2] T. Geng, Y. Lv, B. Wu, X. Zhang, and H. Wen, "Reservoir evaluation method and development countermeasures for fracture-vuggy reservoir," *Special Oil and Gas Reservoirs*, vol. 28, pp. 129–136, 2021.

[3] B. Liu, Y. Jin, and M. Chen, "Influence of vugs in fractured-vuggy carbonate reservoirs on hydraulic fracture propagation based on laboratory experiments," *Journal of Structural Geology*, vol. 124, pp. 143–150, 2019.

[4] J. Guo, L. Zhan, B. Gou et al., "Formation of fractures in carbonate rocks by pad acid fracturing with different states of carbon dioxide," *Petroleum Exploration and Development*, vol. 48, no. 3, pp. 744–751, 2021.

[5] Y. Guo, P. Deng, C. Yang, X. Chang, L. Wang, and J. Zhou, "Experimental investigation on hydraulic fracture propagation of carbonate rocks under different fracturing fluids," *Energies*, vol. 11, no. 12, p. 3502, 2018.

[6] B. Luo, J. Guo, W. Fu, C. Lu, J. Zeng, and L. Liu, "Experimental investigation of shear slippage behavior in naturally fractured carbonate reservoirs using X-ray CT," *International Journal of Rock Mechanics and Mining Sciences*, vol. 122, article 104066, 2019.

[7] Z. Liu, S. Wang, H. Zhao et al., "Effect of random natural fractures on hydraulic fracture propagation geometry in fractured

carbonate rocks," *Rock Mechanics and Rock Engineering*, vol. 51, no. 2, pp. 491–511, 2018.

[8] B. Gou, L. Zhan, J. Guo et al., "Effect of different types of stimulation fluids on fracture propagation behavior in naturally fractured carbonate rock through CT scan," *Journal of Petroleum Science and Engineering*, vol. 201, article 108529, 2021.

[9] R. Zhang, B. Hou, B. Zhou, Y. Liu, Y. Xiao, and K. Zhang, "Effect of acid fracturing on carbonate formation in Southwest China based on experimental investigations," *Journal of Natural Gas Science and Engineering*, vol. 73, article 103057, 2020.

[10] B. Hou, R. Zhang, P. Tan et al., "Characteristics of fracture propagation in compact limestone formation by hydraulic fracturing in central Sichuan, China," *Journal of Natural Gas Science and Engineering*, vol. 57, pp. 122–134, 2018.

[11] Z. Liu, M. Chen, and G. Zhang, "Analysis of the influence of a natural fracture network on hydraulic fracture propagation in carbonate formations," *Rock Mechanics and Rock Engineering*, vol. 47, no. 2, pp. 575–587, 2014.

[12] Y. Dai, B. Hou, C. Zhou, K. Zhang, and F. Liu, "Interaction law between natural fractures-vugs and acid-etched fracture during steering acid fracturing in carbonate reservoirs," *Geofluids*, vol. 2021, Article ID e6649874, 16 pages, 2021.

[13] J. Qiao, X. Tang, M. Hu, J. Rutqvist, and Z. Liu, "The hydraulic fracturing with multiple influencing factors in carbonate fracture-cavity reservoirs," *Computers and Geotechnics*, vol. 147, article 104773, 2022.

[14] Y. Chen, G. Ma, T. Li, Y. Wang, and F. Ren, "Simulation of wormhole propagation in fractured carbonate rocks with unified pipe-network method," *Computers and Geotechnics*, vol. 98, pp. 58–68, 2018.

[15] I. Shovkun and D. N. Espinoza, "Fracture propagation in heterogeneous porous media: pore-scale implications of mineral dissolution," *Rock Mechanics and Rock Engineering*, vol. 52, no. 9, pp. 3197–3211, 2019.

[16] I. Shovkun and D. N. Espinoza, "Propagation of toughness-dominated fluid-driven fractures in reactive porous media," *International Journal of Rock Mechanics and Mining Sciences*, vol. 118, pp. 42–51, 2019.

[17] G. Ma, Y. Chen, Y. Jin, and H. Wang, "Modelling temperature-influenced acidizing process in fractured carbonate rocks," *International Journal of Rock Mechanics and Mining Sciences*, vol. 105, pp. 73–84, 2018.

[18] G. Ma, Y. Chen, H. Wang, T. Li, and W. Nie, "Numerical analysis of two-phase acidizing in fractured carbonate rocks," *Journal of Natural Gas Science and Engineering*, vol. 103, p. 104616, 2022.

[19] S. Li, Y. Kang, L. You, D. Li, and Z. Lian, "Experimental and numerical investigation of multiscale fracture deformation in fractured–vuggy carbonate reservoirs," *Arabian Journal for Science and Engineering*, vol. 39, no. 5, pp. 4241–4249, 2014.

[20] Z. Luo, N. Zhang, L. Zhao, N. Li, D. Ren, and F. Liu, "An extended finite element method for the prediction of acid-etched fracture propagation behavior in fractured-vuggy carbonate reservoirs," *Journal of Petroleum Science and Engineering*, vol. 191, article 107170, 2020.

[21] D. Wang, F. Zhou, W. Ding et al., "A numerical simulation study of fracture reorientation with a degradable fiber-diverting agent," *Journal of Natural Gas Science and Engineering*, vol. 25, pp. 215–225, 2015.

[22] D. Wang, S. Zlotnik, P. Díez, H. Ge, F. Zhou, and B. Yu, "A numerical study on hydraulic fracturing problems via the proper generalized decomposition method," *Computer Modeling in Engineering and Sciences*, vol. 122, no. 2, pp. 703–720, 2020.

[23] D. Wang, Y. Dong, D. Sun, and B. Yu, "A three-dimensional numerical study of hydraulic fracturing with degradable diverting materials via CZM-based FEM," *Engineering Fracture Mechanics*, vol. 237, article 107251, 2020.

[24] X. Yan, D. Wang, C. Zheng et al., "Numerical investigation of hydraulic fracture propagation in heterogeneous rocks using the damage mechanics model," *Journal of Porous Media*, vol. 25, 2022.

[25] T. Wang, Y. Wang, Y. Peng et al., "Simulation and evaluation for acid fracturing of carbonate reservoirs based on embedded discrete fracture model," *Natural Gas Industry B*, vol. 8, no. 6, pp. 637–649, 2021.

[26] C. H. Yew and X. Weng, *Mechanics of Hydraulic Fracturing*, Gulf Professional Publishing, Amsterdam, 2nd edition edition, 2014.

[27] G. Zhang and M. Chen, "Comprehensive mechanical model of reservoirs of carbonate salt rock after acid fracturing damage and its application," *Chinese Journal of Rock Mechanics and Engineering*, vol. S2, pp. 3458–3463, 2009.